A Fast Numerical Method for the Interfacial Motion of an Electrically Conducting Bubble in a Stokes Flow

by

Allan Majdanac

B.Sc., Simon Fraser University, 2001

M.A.Sc., University of British Columbia, 2004

A THESIS SUBMITTED IN PARTIAL FULFILLMENT
OF THE REQUIREMENTS FOR THE DEGREE OF
MASTER OF SCIENCE
IN THE DEPARTMENT
OF
MATHEMATICS

SIMON FRASER UNIVERSITY
Fall 2008

APPROVAL

Name: Allan Majdanac

Degree: Master of Science

Title of thesis: A Fast Numerical Method for the Interfacial Motion of an Electrically Conducting Bubble in a Stokes Flow

Examining Committee: Dr. Razvan Fetecau
Chair

Dr. Mary-Catherine A. Kropinski
Senior Supervisor

Dr. David J. Muraki
Committee Member

Dr. J.F. Williams
Internal Examiner

Date Approved: _____

Abstract

There is a great need for efficient numerical methods when solving interfacial motion problems involving coupled physical processes. To this end, a fast numerical method is developed for tracking the motion of an electrically conducting fluid bubble in a Stokes flow subject to an electric field.

The motion of a two-dimensional bubble immersed in an infinite expanse of viscous fluid is examined. The Stokes equations governing the fluid dynamics and Laplace's equation governing the electrostatics are recast as integral equations. The electrohydrodynamic free boundary problem is reduced to the solution of integral equations along the bubble interface. The integral equations are discretized and solved with an iterative solver accelerated by the fast multipole method. Results from the numerical method are compared with published results of a simplified, analytical model and are found to be in good agreement.

Key Words: Stokes flows, electrohydrodynamics, fluid interfaces, integral equations, fast multipole methods.

Acknowledgments

I'd like to thank my supervisor, Dr. Mary-Catherine Kropinski, for all her encouragement during the course of my studies at SFU. She taught the first fluid dynamics course I ever took, and it inspired me to choose the subject as my field of study. Of the several fluids courses I've taken over the years, hers was the best, most practical, and most informative one by far. I could not have asked for a better foundation in fluid dynamics. In addition, her support as my supervisor has been outstanding. From my time as a summer research student, to my graduate studies, she has always been gracious enough to let me learn from her. With all of the stalls and delays in starting and finishing my masters degree, it was her patience that gave me the time and motivation I needed to complete. I could not have had a better supervisor.

I'd also like to thank Dr. David Muraki for all of his guidance through the years. The long talks I've had with him over all things mathematical have been very useful in steering me along my career path in life. His dedication to students both in and out of the classroom is amazing, and he is an excellent role model for any young mathematician.

I'd like to thank my wife for her support and patience with me as I once again neglected her in favour of another degree. I now gladly begin my hiatus from formal education, in order to be a better husband to her and to be a father to our new son.

Contents

Approval **ii**

Abstract **iii**

Acknowledgments **iv**

Contents **v**

List of Tables **viii**

List of Figures **ix**

1 Introduction **1**

2 Mathematical Model **4**

2.1 Fluid Dynamical Model 4

2.2 Electrostatic Model 5

2.3 Boundary Conditions 6

2.3.1 Dynamic Boundary Condition 6

2.3.2 Kinematic Boundary Condition 8

2.3.3 Far-Field Boundary Condition 8

2.3.4 Electrostatic Boundary Conditions 9

2.4 Dimensionless Problem Formulation 9

3 Complex Variable Reformulation **12**

3.1 Fluid Problem Reformulation 12

3.2 Boundary Condition Reformulation 14

3.2.1 Dynamic Boundary Condition Reformulation 14
3.2.2 Kinematic Boundary Condition Reformulation 17
3.2.3 Far-Field Boundary Condition Reformulation 17

4 Integral Equation Reformulation **19**
4.1 Fluid Problem 19
4.2 Electrostatic Boundary Value Problem 21
4.2.1 Boundary Integral Reformulation 21
4.2.2 Dirichlet-Neumann Map 24

5 Numerical Methods **26**
5.1 Numerical Stokes Flow Solver 26
5.1.1 Equal Arclength Parameterization 26
5.1.2 Spectral Discretization 28
5.1.3 Numerical Solution of Integral Equations 29
5.1.4 Time Discretization 31
5.2 Numerical Electrostatic Solver 32
5.2.1 Discretization of Integral Equation 32
5.2.2 Discretization of Harmonic Conjugate 34
5.3 Test Cases 35
5.3.1 Test Case - Calculation of Potential 35
5.3.2 Test Case - Principal Value Integrals and Derivative of Harmonic Conjugate 38

6 Electrohydrodynamic Bubble Problem **40**
6.1 Analytical Solution Method 41
6.1.1 Complex Variable Reformulation 41
6.1.2 Conformal Mapping 42
6.2 Crowdy's Results 44
6.2.1 Sub-Critical Case 44
6.2.2 Super-Critical Case 47
6.3 Numerical Test Cases and Comparison 48
6.3.1 Sub-Critical Case 48
6.3.2 Super-Critical Case 54

7 Conclusion and Future Work **55**

7.1 Conclusion 55

7.2 Future Work 56

Bibliography **58**

List of Tables

5.1 Errors for Potential Test Case, $a = 1$, $b = 2$ 37
5.2 Errors for Potential Test Case, $a = 1, b = 5$ 37
5.3 Error ratios for Harmonic Conjugate Test Cases, $a = 3, b = 1$ 39

6.1 CPU times for elliptical bubble profile, $a = 1.44$, $b = 0.6942$, $\Delta t = 0.001$. . . . 52

List of Figures

2.1 Geometry Of Bubble 4

5.1 Geometry for Exterior Dirichlet Problem, $a = 1, b = 2$ 35
5.2 Geometry for Exterior Dirichlet Problem, $a = 1, b = 5$ 36
5.3 Errors for Potential Test Case, $a = 1, b = 2$ 36
5.4 Errors for Potential Test Case, $a = 1, b = 5$ 37
5.5 Errors for Harmonic Conjugate Test Cases, $a = 3, b = 1$ 39

6.1 Equilibrium bubble profiles evolving from an initially circular profile, showing $E = \sqrt{\beta} = 0.5, 0.65, 0.73$. 45
6.2 Graph of E^2 vs. e showing critical equilibrium value of $E = \sqrt{\beta}$=0.7372. . . . 47
6.3 Non-equilibrium bubble profile for super-critical case. 47
6.4 Comparison of computed profile vs. Crowdy model, $E = \sqrt{\beta} = 0.5$. 48
6.5 Scaling relationship between solver and evolution model. 49
6.6 Comparison of Crowdy model, $E = 0.40$ vs. computed profile, $\sqrt{\beta} = 0.566$. . 50
6.7 Comparison of Crowdy model, $E = 0.50$ vs. computed profile, $\sqrt{\beta} = 0.707$. . 51
6.8 Comparison of Crowdy model, $E = 0.60$ vs. computed profile, $\sqrt{\beta} = 0.849$. . 51
6.9 Comparison of Crowdy model, $E = 0.73$ vs. computed profile, $\sqrt{\beta} = 1.032$. . 52
6.10 Comparison of computed profile for $\beta = 9.0$ and an ellipse. 53
6.11 Comparison of maximum equilibrium profiles. Computed, $\beta = 15.0$ vs. Crowdy, $E = 0.7372$. 53
6.12 Computed profiles showing bubble pinch-off, $\beta = 50$, $N = 1024$. 54

Chapter 1

Introduction

Bubbles and drops are common phenomena both in everyday life and in scientific applications. Due to their ubiquity, there is great interest in understanding how they behave in various situations. For example, in order to print material onto a page with an ink-jet printer, an electrically conducting fluid drop is subjected to an electric field. The physical processes involved in an example such as this are fairly complex. In addition to the fluid dynamics governing the drop, the electric field adds further complexity by coupling electrostatic effects to the fluid dynamics. This simple example illustrates that the behavior of a conducting drop within an electrohydrodynamic context is of practical use. A mathematical description of the processes involved is a useful tool in improving understanding of applications such as this.

In general, electrohydrodynamic bubble and drop problems have been studied for quite some time. Wilson & Taylor [37] first studied problems involving conducting drops from an experimental point of view. They found that, in addition to unsteady time-dependent drop profiles, steady-state equilibrium profiles existed for certain electric field strengths. As summarized in Dubash & Mestel [10], several authors subsequently performed three-dimensional analytical studies in an attempt to model the equilibrium shape, using spheroidal or axisymmetric approximations for the drop profile. In an extension of the work in [37], many authors experimentally studied the equilibrium behavior for various fluid viscosities and found that both the electric field strength and the viscosity ratio of the fluids used had a significant effect on the equilibrium profile. However, these studies dealt mainly with cases where the drop viscosity was relatively high, and there appear to be no studies that dealt with inviscid bubbles in viscous fluids.

The time dependent deformation problem is more challenging. Analytic studies have focused mainly on bubble deformation without electrostatic effects. Tanveer & Vasconcelos [33] examined two-dimensional bubbles in a Stokes flow regime under the influence of an external straining flow, while Siegel [31, 32] extended the work to included surfactants on the bubble interface. Most recently, Crowdy [8] extended the work of Tanveer & Vasconcelos to include electrostatic effects in a two-dimensional Stokes flow framework. This appears to be the only published work dealing with the electrohydrodynamic bubble problem for two-dimensional Stokes flow. Crowdy's results show that the bubble achieves steady-state profiles and non-equilibrium profiles, analogous to the three-dimensional experimental results reported in Wilson & Taylor.

For the three-dimensional time dependent problem, Sherwood [30] used a numerical approach based on boundary integrals to study drop deformation of equal viscosity fluids. It was not until very recently that a three-dimensional numerical study of the electrohydrodynamic bubble problem was undertaken by Dubash & Mestel [9, 10, 11]. Their work considered an inviscid bubble deforming within a viscous fluid in Stokes flow. The study used a numerical method based on a boundary integral formulation by Pozrikidis [28, 29]. The simulations showed that the bubble achieved both steady-state profiles and non-equilibrium profiles as predicted by the original experiments of Wilson & Taylor.

Using numerical methods, there has been progress toward understanding the behavior of an electrohydrodynamic conducting bubble. However, from the point of view of computational efficiency, there is still much to be desired from the existing studies. For instance, the numerical method employed by Dubash & Mestel uses a direct solver for the resulting system of linear equations obtained from discretization of the boundary integral equations. As is well known, the number of floating point operations needed to solve a linear system via direct methods is $\mathcal{O}(N^3)$, where N is the number of points used to discretize the boundary. For most cases, in order to properly resolve a bubble interface, hundreds, if not thousands, of points are needed. This makes the computational cost of using direct solvers prohibitively high. If the problem is extended to deal with several bubbles, direct solvers are completely inadequate due to this high cost. To solve time dependent electrohydrodynamic bubble problems over long time scales, the need for efficient numerical methods becomes paramount.

To this end, the goal of this thesis is to develop a fast and efficient numerical method for tracking the interfacial motion of a fluid bubble subject to an electric field. This thesis

builds from the work of Kropinski [20], where fast numerical methods were developed for solving two-dimensional interfacial Stokes flow problems. These methods make use of integral equations and solve the linear systems arising from discretization with an iterative solver accelerated by the fast multipole method. The result is a method that is able to solve complex interfacial motion problems in $\mathcal{O}(N)$ floating point operations. These methods have been used to compute large-scale, time dependent bubble deformation problems [19, 20, 21, 24]. They offer tremendous savings in computational cost over direct solvers, and even standard iterative solvers. Clearly, the power of these numerical methods for solving interfacial problems is apparent, and they are efficient tools for investigating the behavior of various interfacial problems.

Specifically, this thesis develops a method for simulating the interfacial motion of a two-dimensional conducting bubble placed in an infinite expanse of viscous fluid. The bubble is subject to an externally applied uniform electric field. In Chapter 2, the mathematical model consisting of the governing equations and boundary conditions are stated in a primitive variable formulation. In Chapter 3, the equations are rewritten in a complex variable formulation by taking advantage of the two-dimensional nature of the problem. Analytic function theory is used in an attempt to solve the problem in a more elegant manner. In Chapter 4, the complex variable statement of the problem is rewritten in terms of integral equations along the bubble interface. Since the problem is too complicated to admit an analytic solution, a numerical approach is adopted. These integral equations are more amenable to solution by numerical methods. In Chapter 5, the equations are discretized and the procedure used to solve them is discussed. Several test cases are presented to verify the correct implementation of the solver. In Chapter 6 the numerical solver is used to compute solutions to the electrohydrodynamic bubble problem. Concluding remarks and suggestions for future research are discussed in Chapter 7.

Chapter 2

Mathematical Model

2.1 Fluid Dynamical Model

Consider a closed interface in an unbounded expanse of viscous fluid in two-dimensional space. The interface or *bubble* encloses a fluid with negligible viscosity and negligible density. The motion of fluid within the bubble is of no interest. The case of an interface enclosing a fluid with non-negligible viscosity is called a *drop*, and is not considered in this study. The internal pressure of the bubble p_b is assumed spatially constant, but may change in time. The viscosity of the external fluid is constant and given by μ. The unbounded region is denoted by Ω, while the interface is denoted by $\partial\Omega$.

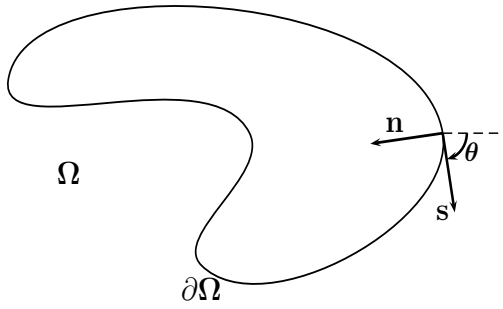

Figure 2.1: Geometry Of Bubble

The velocity of the external fluid is given by $\mathbf{u}(\mathbf{x}, t)$ and the pressure is given by $p(\mathbf{x}, t)$. The external fluid is an incompressible Newtonian fluid and it is assumed that the flow within Ω is dominated by viscous effects. Therefore, the equations governing the motion of

the fluid within Ω are the *Stokes equations* and the *continuity equation*

$$\mu\Delta\mathbf{u} = \nabla p \tag{2.1}$$

$$\nabla\cdot\mathbf{u} = 0. \tag{2.2}$$

Equation (2.2) states that the velocity field is solenoidal in Ω and can be rewritten in terms of a vector potential, which in two-dimensions is expressed as $\mathbf{u} = \nabla\times\Psi\hat{\mathbf{k}}$. The function $\Psi = \Psi(\mathbf{x}, t)$ is the called the *stream function*. Equation (2.2) implies the following relationship in $\mathbb{R}^2$ between the stream function and the velocity components $\mathbf{u}(\mathbf{x}, t) = u(\mathbf{x}, t)\hat{\mathbf{i}} + v(\mathbf{x}, t)\hat{\mathbf{j}}$

$$u = \frac{\partial\Psi}{\partial y}, \tag{2.3}$$

$$v = -\frac{\partial\Psi}{\partial x}. \tag{2.4}$$

Note that the stream function identically satisfies the equation of continuity, (2.2). Using the vector identity $\Delta\mathbf{u} = \nabla(\nabla\cdot\mathbf{u}) - \nabla\times\nabla\times\mathbf{u}$ and (2.2), (2.1) is written as

$$-\mu\nabla\times\nabla\times\mathbf{u} = \nabla p. \tag{2.5}$$

Taking the curl of (2.5) and using the above vector identity gives $\Delta(\nabla\times\mathbf{u}) = \mathbf{0}$. Noting that $\mathbf{u} = \nabla\times\Psi\hat{\mathbf{k}}$, and using the vector identity a third time, (2.5) becomes

$$\begin{aligned}\Delta(\Delta\Psi\hat{\mathbf{k}}) &= \mathbf{0}\\ \implies \Delta^2\Psi &= 0.\end{aligned} \tag{2.6}$$

The Stokes equations for the velocity and pressure become a single scalar partial differential equation in terms of the stream function, known as the *biharmonic equation*.

2.2 Electrostatic Model

In addition to the fluid dynamics, a uniform electric field $\mathbf{E} = E_0\hat{\mathbf{i}}$ is applied to both the bubble and external fluid simultaneously. It is assumed that the interface between the bubble and the external fluid, denoted by $\partial\Omega$, is both electrically uncharged and a perfectly conducting surface. In addition, it is assumed that the fluids carry no electric charge and are perfectly insulating. The electrostatic behavior of this system is governed by Maxwell's

equations. Since there are no charges in either the bubble or the external fluid, Maxwell's equations reduce to

$$\nabla \times \mathbf{E} = \mathbf{0}, \tag{2.7}$$

$$\nabla \cdot \mathbf{E} = 0. \tag{2.8}$$

Equation (2.7) states that the electric field is irrotational in $\mathbb{R}^2$, implying the existence of a scalar electric potential ϕ in $\mathbb{R}^2$ (and Ω). Physical arguments motivate $\mathbf{E} = -\nabla\phi$ as the definition of the electric potential [7]. According to (2.8), ϕ satisfies Laplace's equation in $\mathbb{R}^2$ (and Ω):

$$\Delta\phi = 0. \tag{2.9}$$

2.3 Boundary Conditions

Equations (2.1), (2.2) govern the fluid dynamical behavior of the problem and (2.9) governs the electrostatic behavior of the problem. The processes are coupled through boundary conditions on the bubble surface.

2.3.1 Dynamic Boundary Condition

The electrostatic effects are coupled to the fluid dynamics through stresses on the bubble interface, which are described in terms of components normal and tangent to the interface. In general, pressure, viscous, and electric stresses act on the bubble interface, and these are balanced by forces due to surface tension. It is assumed that the interface has a variable surface tension coefficient $\sigma = \sigma(\mathbf{x}, t)$. The normal and tangential stress balances are combined [29] to give the equation

$$-(p - p_b)n_i + \left[(\tau_{ij} + T_{ij}) - (\tau_{ij} + T_{ij})_b\right] n_j = \sigma\kappa n_i + s_k \frac{\partial\sigma}{\partial x_k} s_i. \tag{2.10}$$

The subscript b refers to quantities inside the bubble. Here, $s_i = \mathbf{s}$ is a unit tangent vector to the interface. The orientation is such that the external domain Ω lies to the left of the interface, so $\mathbf{s}$ moves in a clockwise direction about the bubble. The outward unit normal vector to the interface is given by $n_i = \mathbf{n}$ and points into the bubble, as Ω is the domain of interest. This geometry is illustrated in Figure 2.1. The curvature of the interface at a

given point is κ, τ is the viscous stress tensor for incompressible Newtonian fluids, and T is the Maxwell electric stress tensor [15]

$$\tau_{ij} = \mu\left(\frac{\partial u_i}{\partial x_j} + \frac{\partial u_j}{\partial x_i}\right), \tag{2.11}$$

$$T_{ij} = \varepsilon_0\left(E_iE_j - \tfrac{1}{2}\delta_{ij}|\mathbf{E}|^2\right). \tag{2.12}$$

The following conditions apply to the bubble

- The internal bubble pressure is constant and set to zero without loss of generality.
- The fluid in the bubble has negligible viscosity.
- The electric field inside a perfect conductor is zero [7] (*i.e.*, $(T_{ij})_b = 0$).

Using these conditions, (2.10) simplifies to

$$-pn_i + (\tau_{ij} + T_{ij})n_j = \sigma\kappa n_i + s_k\frac{\partial\sigma}{\partial x_k}s_i. \tag{2.13}$$

In (2.13) the electric stress term, $T_{ij}n_j$, is rewritten as

$$\begin{aligned} T_{ij}n_j &= \varepsilon_0\left(E_iE_j - \tfrac{1}{2}\delta_{ij}|\mathbf{E}|^2\right)n_j \\ &= \varepsilon_0\left(E_iE_jn_j - \tfrac{1}{2}|\mathbf{E}|^2n_i\right) \\ &= \varepsilon_0\left(E_i(\mathbf{E}\cdot\mathbf{n}) - \tfrac{1}{2}|\mathbf{E}|^2n_i\right) \\ &= \varepsilon_0\left((\mathbf{E}\cdot\mathbf{n})\mathbf{E} - \tfrac{1}{2}|\mathbf{E}|^2\mathbf{n}\right). \end{aligned}$$

The electric field is decomposed tangentially and normally relative to the bubble interface

$$\mathbf{E} = (\mathbf{E}\cdot\mathbf{s})\mathbf{s} + (\mathbf{E}\cdot\mathbf{n})\mathbf{n}.$$

Since the interface is a perfect conductor, the electric field at the bubble surface is everywhere normal to the surface [7] giving $\mathbf{E} = (\mathbf{E}\cdot\mathbf{n})\mathbf{n}$ for $\mathbf{x}\in\partial\Omega$. The electric stress becomes

$$\begin{aligned} T_{ij}n_j &= \varepsilon_0\left((\mathbf{E}\cdot\mathbf{n})\mathbf{E} - \tfrac{1}{2}|\mathbf{E}|^2\mathbf{n}\right) \\ &= \varepsilon_0\left((\mathbf{E}\cdot\mathbf{n})^2\mathbf{n} - \tfrac{1}{2}|(\mathbf{E}\cdot\mathbf{n})\mathbf{n}|^2\mathbf{n}\right) \\ &= \frac{\varepsilon_0}{2}(\mathbf{E}\cdot\mathbf{n})^2\mathbf{n}. \end{aligned}$$

The electric field is written in terms of the potential and substituted into the above expression

$$\begin{aligned} T_{ij}n_j &= \frac{\varepsilon_0}{2}(\mathbf{E}\cdot\mathbf{n})^2\mathbf{n} \\ &= \frac{\varepsilon_0}{2}(-\nabla\phi\cdot\mathbf{n})^2\mathbf{n} \\ &= \frac{\varepsilon_0}{2}\left(\frac{\partial\phi}{\partial n}\right)^2\mathbf{n}. \end{aligned} \tag{2.14}$$

Equation (2.14) shows that there is no tangential electric field on the bubble surface, so the only coupling of the electric field to the external fluid is through a normally directed electric stress. The stress balance at the interface (2.13) is given by

$$-pn_i + \tau_{ij}n_j + \frac{\varepsilon_0}{2}\left(\frac{\partial\phi}{\partial n}\right)^2 n_i = \sigma\kappa n_i + s_k\frac{\partial\sigma}{\partial x_k}s_i. \tag{2.15}$$

2.3.2 Kinematic Boundary Condition

As formulated in (2.1) and (2.9), the fluid dynamics and the electrostatic problem are in steady-state. However, the interface location does change in time due to variations in the stresses acting on the surface. Therefore, this is a quasi-static free-boundary problem and the interface evolves according to the kinematic boundary condition at the bubble surface. The points that make up the interface, $\mathbf{x}\in\partial\Omega$, move with a velocity equal to the normal velocity of the interface. Since the interface moves under the influence of the external fluid only, this condition is given by

$$\frac{d\mathbf{x}}{dt} = (\mathbf{u}\cdot\mathbf{n})\mathbf{n}. \tag{2.16}$$

2.3.3 Far-Field Boundary Condition

The velocity and pressure of the external fluid must satisfy boundary conditions as $|\mathbf{x}|\to\infty$. These conditions are discussed in detail within [14, 24, 33] and repeated here for completeness only. In the far-field, the velocity is asymptotic to the following

$$\mathbf{u}\sim\mathbf{u}_\infty + \mathcal{O}\left(\frac{1}{|\mathbf{x}|^2}\right), \tag{2.17}$$

where

$$\mathbf{u}_\infty = \frac{1}{2}\begin{pmatrix} \alpha_0 & \beta_0-\omega_\infty \\ \beta_0+\omega_\infty & -\alpha_0 \end{pmatrix}\cdot\mathbf{x}.$$

Here ω_∞ is the far-field vorticity of the fluid, while α_0, β_0 characterize the strain rate of the flow. For a quiescent external fluid, these constants are all equal to zero. The pressure in the far-field is given by

$$p \sim p_\infty + \mathcal{O}\left(\frac{1}{|\mathbf{x}|^2}\right), \tag{2.18}$$

where the far-field pressure p_∞ is a constant that is determined as part of the solution to the problem.

2.3.4 Electrostatic Boundary Conditions

Since the interface is perfectly conducting, the electric field inside the bubble is zero [7]. This implies that the interface is an equi-potential surface and $\phi = 0$ is taken on $\partial\Omega$ without loss of generality. In addition, the presence of the conducting bubble alters the uniform electric field in the external fluid. However, the bubble has a diminishing influence in the far-field. Hence, the electric field approaches the uniform field as $|\mathbf{x}| \to \infty$, so $\phi \to -E_0 x$ as $|\mathbf{x}| \to \infty$. The electric potential satisfies the following Dirichlet problem in Ω:

$$\begin{cases} \Delta\phi = & 0, & \mathbf{x} \in \Omega \\ \phi = & 0, & \mathbf{x} \in \partial\Omega \\ \phi \to & -E_0 x, & \text{as } |\mathbf{x}| \to \infty. \end{cases} \tag{2.19}$$

To produce a bounded solution in the far-field, (2.19) is rewritten using a disturbance electric potential, $\tilde{\phi} = E_0 x + \phi$. This results in the following Dirichlet problem

$$\begin{cases} \Delta\tilde{\phi} = & 0, & \mathbf{x} \in \Omega \\ \tilde{\phi} = & E_0 x, & \mathbf{x} \in \partial\Omega \\ \tilde{\phi} \to & 0, & \text{as } |\mathbf{x}| \to \infty. \end{cases} \tag{2.20}$$

Once (2.20) is solved for $\tilde{\phi}$, the original potential ϕ is recovered from $\phi = \tilde{\phi} - E_0 x$.

2.4 Dimensionless Problem Formulation

All variables and functions are non-dimensionalized according to the following conventions. The characteristic length scale R is the length of the region bounded by the interface $\partial\Omega$, which is taken as the diameter of the bubble. σ_0 is a characteristic surface tension coefficient value, μ_0 is a characteristic viscosity value for the external fluid, and E_0 is the strength of the

externally applied electric field. Quantities with hats are dimensional, while those without are dimensionless and are defined as

$$\begin{aligned} x_i &= \frac{\hat{x_i}}{R} & t &= \frac{\hat{t}}{\mu_0 R/\sigma_0} \\ \frac{\partial}{\partial x_i} &= R\frac{\partial}{\partial \hat{x_i}} & \sigma &= \frac{\hat{\sigma}}{\sigma_0} \\ \mathbf{u} &= \frac{\hat{\mathbf{u}}}{\sigma_0/\mu_0} & p &= \frac{\hat{p}}{\sigma_0/R} \\ \phi &= \frac{\hat{\phi}}{E_0 R} & \kappa &= \hat{\kappa} R \end{aligned}$$

Starting from (2.1) and (2.2), using the above non-dimensionalizations, and dropping the hats for convenience, the dimensionless fluid dynamical problem is

$$\Delta \mathbf{u} = \nabla p \tag{2.21}$$

$$\nabla \cdot \mathbf{u} = 0. \tag{2.22}$$

The form of (2.6), the biharmonic equation, is invariant under the non-dimensionalization,

$$\Delta^2 \Psi = 0. \tag{2.23}$$

From (2.20), the dimensionless modified electrostatic boundary value problem is

$$\begin{cases} \Delta\tilde{\phi} = 0, & \mathbf{x} \in \Omega \\ \tilde{\phi} = x, & \mathbf{x} \in \partial\Omega \\ \tilde{\phi} \to 0, & \text{as } |\mathbf{x}| \to \infty. \end{cases} \tag{2.24}$$

The original dimensionless potential ϕ is recovered from $\phi = \tilde{\phi} - x$.

The non-dimensional form of the viscous stress tensor, (2.11), is simply

$$\tau_{ij} = \left(\frac{\partial u_i}{\partial x_j} + \frac{\partial u_j}{\partial x_i} \right). \tag{2.25}$$

Using (2.25) in (2.15) yields the dimensionless dynamic boundary condition

$$-pn_i + \tau_{ij} n_j + \frac{\beta}{2} \left(\frac{\partial \phi}{\partial n} \right)^2 n_i = \sigma \kappa n_i + s_k \frac{\partial \sigma}{\partial x_k} s_i. \tag{2.26}$$

Equation (2.26) contains a single dimensionless parameter, β, given by

$$\beta = \frac{\varepsilon_0 E_0^2 R}{\sigma_0}. \tag{2.27}$$

This parameter represents the ratio of electrostatic forces to surface tension forces and it controls the influence of the electric field on the bubble deformation. This parameter is discussed at length in later sections.

The kinematic boundary condition, (2.16), is invariant under non-dimensionalization,

$$\frac{d\mathbf{x}}{dt} = (\mathbf{u}\cdot\mathbf{n})\mathbf{n}. \tag{2.28}$$

The far-field boundary condition for velocity, (2.17), becomes

$$\mathbf{u} \sim \mathbf{u}_\infty + \mathcal{O}\left(\frac{1}{|\mathbf{x}|^2}\right), \tag{2.29}$$

where

$$\mathbf{u}_\infty = \frac{Q}{2}\begin{pmatrix} 1 & (\beta_0-\omega_\infty)/\alpha_0 \\ (\beta_0+\omega_\infty)/\alpha_0 & -1 \end{pmatrix}\mathbf{x}.$$

Here, $Q = \frac{R\mu\alpha_0}{\sigma_0}$ is the *capillary number* and represents the ratio of viscous forces to surface tension forces. Once again, for a stationary external flow, the straining and vorticity constants in the above matrix are zero.

The far-field pressure, (2.18), remains invariant under the non-dimensionalization,

$$p \sim p_\infty + \mathcal{O}\left(\frac{1}{|\mathbf{x}|^2}\right). \tag{2.30}$$

Equations (2.21)-(2.30) constitute the mathematical description of the electrohydrodynamic bubble problem.

Chapter 3

Complex Variable Reformulation

3.1 Fluid Problem Reformulation

Complex variables and analytic function theory are used to rewrite the equations of this coupled free boundary value problem in a form more suitable for solution by integral equation methods. Consider the Stokes equation, (2.21). Taking the divergence of the equation, noting that the laplacian operator commutes with the divergence operator, and invoking the continuity condition, (2.22), shows that the pressure, p, is harmonic in Ω

$$\begin{aligned} \nabla \cdot \nabla p &= \nabla \cdot \Delta \mathbf{u} \\ \implies \Delta p &= 0. \end{aligned}$$

From the relationship between the stream function and the velocity components, (2.3), (2.4), the non-zero component of vorticity in $\mathbb{R}^2$, $\boldsymbol{\omega} = \nabla \times \mathbf{u} = \omega(\mathbf{x}, t)\hat{\mathbf{k}}$, is defined in terms of Ψ

$$\begin{aligned} \Delta\Psi &= \frac{\partial u}{\partial y} - \frac{\partial v}{\partial x} \\ &= -(\nabla \times \mathbf{u}) \cdot \hat{\mathbf{k}} \\ &= -\boldsymbol{\omega} \cdot \hat{\mathbf{k}} \\ \implies \Delta\Psi &= -\omega. \end{aligned}$$

The biharmonic equation, (2.23), implies that the vorticity is harmonic in Ω

$$\begin{aligned} \Delta(\Delta\Psi) &= \Delta(-\omega) \\ &= 0 \\ \implies \Delta\omega &= 0. \end{aligned}$$

Using (2.21) and the definition of vorticity, further examination of p and ω yields the following relationships

$$\begin{aligned} \frac{\partial \omega}{\partial x} &= \frac{\partial p}{\partial y}, \\ \frac{\partial \omega}{\partial y} &= -\frac{\partial p}{\partial x}. \end{aligned} \tag{3.1}$$

At this point, analytic function theory is invoked. To begin with, note that any point $\mathbf{x} = x\hat{\mathbf{i}} + y\hat{\mathbf{j}} \in \mathbb{R}^2$ is equivalent to a corresponding point $z = x + iy \in \mathbb{C}$. Therefore, $\omega(\mathbf{x}, t) = \omega(z, t)$, *etc.* These notations are interchanged at will and no further distinction is made between $\mathbb{R}^2$ and $\mathbb{C}$. With this in mind, (3.1) is a statement of the Cauchy-Riemann equations for p and ω. Since both p and ω are harmonic in Ω and satisfy the Cauchy-Riemann equations, they can be considered as either the real or the imaginary parts of an analytic function [5]. However, (3.1) shows p and ω are harmonic conjugates in Ω, so they are written as the real and imaginary parts of the same arbitrary analytic function $h(z)$

$$h(z) = \omega(z) + ip(z). \tag{3.2}$$

Here the time dependence of the functions is notationally suppressed, *i.e.*, $\omega(z) = \omega(z, t)$. Since the derivative or anti-derivative of an analytic function is also analytic, the function $h(z)$ in (3.2) is redefined in terms of another analytic function, $h(z) = -4f'(z)$. Here the prime notation indicates differentiation with respect to z, $f'(z) = \partial f(z, t)/\partial z$. The factor of -4 is chosen for convenience.

Let $f(z) = \int f'(z)dz = P(z) + iQ(z)$ and note that for this analytic function, the Cauchy-Riemann equations give

$$\begin{aligned} \frac{\partial P}{\partial x} &= \frac{\partial Q}{\partial y}, \\ \frac{\partial P}{\partial y} &= -\frac{\partial Q}{\partial x}. \end{aligned} \tag{3.3}$$

Now, note that $\mathrm{Re}(\bar{z}f(z)) = xP + yQ$ and define $G(z) = -\mathrm{Re}(\bar{z}f(z)) + \Psi$. Then, noting that P and Q are harmonic functions, and using (3.1) and (3.3) gives

$$\begin{aligned} \Delta G &= -\Delta(xP + yQ) + \Delta\Psi \\ &= -4\mathrm{Re}(f'(z)) - x\Delta P - y\Delta Q + \Delta\Psi \\ &= \omega + \Delta\Psi \\ &= 0. \end{aligned}$$

Therefore, $G(z)$ is a harmonic function and is written as the real part of another analytic function $g(z)$

$$\begin{aligned} -\mathrm{Re}(\bar{z}f(z)) + \Psi &= \mathrm{Re}(g(z)) \\ \implies \Psi(z) &= \mathrm{Re}(\bar{z}f(z) + g(z)). \end{aligned} \tag{3.4}$$

The functions $f(z)$, $g(z)$ are called *Goursat functions* and serve as complex potentials for the biharmonic function Ψ. It is easily verified that any function of the form (3.4) satisfies the biharmonic equation.

With the introduction of these functions, the goal of the problem is no longer to solve the governing equations (2.21) and (2.22) for velocity and pressure, subject to the boundary conditions (2.26)-(2.30). Instead, the aim is to determine the potentials f and g such that appropriate boundary conditions on these functions are satisfied. These boundary conditions are obtained by reformulating the existing boundary conditions, (2.26)-(2.30), in terms of the Goursat functions. Using this reformulation, the functions are found from the solution of a boundary integral equation, which is discussed in a subsequent section. Once f and g are determined, they are used in (3.4) to obtain the stream function Ψ, which in turn is used to determine the velocity and pressure.

Note however, that the electrostatic potential is required in the dynamic boundary condition, (2.26), and it is not included in the Goursat reformulation. The potential is obtained independently of the Goursat functions through the solution of the boundary value problem (2.24). The resulting solution for ϕ is incorporated into the reformulation of the dynamic boundary condition (2.26) which is then used to determine the Goursat functions.

3.2 Boundary Condition Reformulation

3.2.1 Dynamic Boundary Condition Reformulation

Using the Goursat functions, the terms appearing in the dynamic boundary condition, (2.26), are rewritten in complex variable form [22]. The velocity is given by

$$\begin{aligned} i(u+iv) &= \frac{\partial \Psi}{\partial x} + i\frac{\partial \Psi}{\partial y} \\ &= f(z) + z\overline{f'(z)} + \overline{g'(z)}. \end{aligned} \tag{3.5}$$

Note the notation $\overline{f(z)} = \bar{f}(z)$. From (3.2), the pressure is given simply as

$$p = -4\mathrm{Im}(f'(z)). \tag{3.6}$$

The normal vector to Ω, $\mathbf{n} = n_1\hat{\mathbf{i}} + n_2\hat{\mathbf{j}}$ or $n = n_1 + in_2$, points into the bubble and is given by

$$\begin{aligned} n &= \frac{\partial y}{\partial s} - i\frac{\partial x}{\partial s} \\ &= -i\frac{\partial z}{\partial s}. \end{aligned} \tag{3.7}$$

Here, differentiation is with respect to arclength along the interface. Using (3.6) and (3.7), the pressure stress term, $-pn_i$, in complex form is

$$\begin{aligned} -pn_i &= -4\mathrm{Im}(f'(z))\left(-i\frac{\partial z}{\partial s}\right) \\ &= -4\left(\frac{f'(z) - \overline{f'(z)}}{2i}\right)\left(-i\frac{\partial z}{\partial s}\right) \\ &= 2\left(f'(z) - \overline{f'(z)}\right)\left(\frac{\partial z}{\partial s}\right). \end{aligned} \tag{3.8}$$

The viscous stress term, $\tau_{ij}n_j$, is required. From (2.25), note that $\tau_{12} = \tau_{21}$, and by continuity, (2.22), $\tau_{22} = -\tau_{11}$. The viscous stress is

$$\begin{aligned} \tau_{ij}n_j &= \begin{pmatrix} \tau_{11} & \tau_{12} \\ \tau_{21} & \tau_{22} \end{pmatrix}\begin{pmatrix} n_1 \\ n_2 \end{pmatrix} \\ &= \begin{pmatrix} \tau_{11}n_1 + \tau_{12}n_2 \\ \tau_{21}n_1 + \tau_{22}n_2 \end{pmatrix} \\ &= \begin{pmatrix} \tau_{11}n_1 + \tau_{12}n_2 \\ \tau_{12}n_1 - \tau_{11}n_2 \end{pmatrix} \\ &= (\tau_{11}n_1 + \tau_{12}n_2) + i(\tau_{12}n_1 - \tau_{11}n_2) \\ &= (\tau_{11} + i\tau_{12})(n_1 - in_2) \\ &= (\tau_{11} + i\tau_{12})\bar{n}. \end{aligned} \tag{3.9}$$

Using (2.25) and (3.5), $\tau_{11} + i\tau_{12}$ is

$$\tau_{11} + i\tau_{12} = -2i(z\overline{f''(z)} + \overline{g''(z)}).$$

Therefore, the viscous stress term, (3.9), is

$$\begin{aligned} (\tau_{11} + i\tau_{12})\bar{n} &= -2i\left(z\overline{f''(z)} + \overline{g''(z)}\right)\left(i\overline{\frac{\partial z}{\partial s}}\right) \\ &= 2\left(z\overline{f''(z)} + \overline{g''(z)}\right)\left(\overline{\frac{\partial z}{\partial s}}\right). \end{aligned} \tag{3.10}$$

The surface tension terms in the dynamic boundary condition are also put into complex variable form. The curvature, κ, is defined as

$$\kappa = \frac{d\theta}{ds},$$

where θ is the angle between the tangent to the interface and horizontal, as illustrated in Figure 2.1. The curvature term in the dynamic stress boundary condition is

$$\sigma\kappa n_i = i\sigma\frac{d\theta}{ds}\frac{\partial z}{\partial s}. \tag{3.11}$$

The unit tangent vector, $\mathbf{s} = s_1 + is_2 = s_i$ is written as

$$\begin{aligned} \mathbf{s} &= \frac{\partial x}{\partial s} + i\frac{\partial y}{\partial s} \\ &= \frac{\partial z}{\partial s}. \end{aligned} \tag{3.12}$$

Using (3.12) and writing $\dfrac{\partial z}{\partial s} = e^{i\theta}$ in polar form, (3.11) becomes

$$\begin{aligned} i\sigma\frac{d\theta}{ds}\frac{\partial z}{\partial s} &= \sigma\frac{d\theta}{ds}\frac{d}{d\theta}\left(e^{i\theta}\right) \\ &= \sigma\frac{\partial}{\partial s}\left(e^{i\theta}\right) \\ &= \sigma\frac{\partial^2 z}{\partial s^2}. \end{aligned} \tag{3.13}$$

The tangential surface tension term is also recast into complex form. Using (3.12), the tangential surface tension term becomes

$$s_k\frac{\partial\sigma}{\partial x_k}s_i = \frac{\partial\sigma}{\partial s}\frac{\partial z}{\partial s}. \tag{3.14}$$

Combining the surface tension terms, (3.13) and (3.14), gives

$$\sigma\frac{\partial^2 z}{\partial s^2} + \frac{\partial\sigma}{\partial s}\frac{\partial z}{\partial s} = \frac{\partial}{\partial s}\left(\sigma\frac{\partial z}{\partial s}\right). \tag{3.15}$$

After substituting (3.8), (3.10), and (3.15) into (2.26) and simplifying, the dynamic boundary condition becomes

$$-2\frac{\partial}{\partial s}\left(f(z) - z\overline{f'(z)} - \overline{g'(z)}\right) = \frac{\partial}{\partial s}\left(\sigma\frac{\partial z}{\partial s}\right) + \frac{i\beta}{2}\left(\frac{\partial\phi}{\partial n}\right)^2\frac{\partial z}{\partial s}.$$

Anti-differentiation with respect to arclength, s, gives

$$f(z) - z\overline{f'(z)} - \overline{g'(z)} = -\frac{\sigma}{2}\frac{\partial z}{\partial s} - \frac{i\beta}{4}\int\left(\frac{\partial\phi}{\partial n}\right)^2\frac{\partial z}{\partial s}ds. \tag{3.16}$$

This is the reformulation of the dynamic boundary condition (2.26) in terms of the Goursat functions f and g. As mentioned earlier, the electrostatic potential, ϕ, is determined from the solution of the electrostatic problem (2.24) and $\partial\phi/\partial n$ is computed for use in (3.16). The discussion behind the computation of this normal derivative is deferred to a later section.

3.2.2 Kinematic Boundary Condition Reformulation

The kinematic boundary condition, (2.28), is also written in complex form by noting that $\mathbf{a}\cdot\mathbf{b} = \mathrm{Re}(a\bar{b})$. Using the Goursat representation of velocity, (3.5), and the complex form of the normal vector, (3.7), the kinematic boundary condition becomes

$$\begin{aligned}\frac{dz}{dt} &= \mathrm{Re}(u\bar{n})n \\ &= \mathrm{Re}\left(-i(f(z)+z\overline{f'(z)}+\overline{g'(z)})(i\overline{\partial z/\partial s})\right)(-i\partial z/\partial s) \\ &= -\mathrm{Im}\left((f(z)+z\overline{f'(z)}+\overline{g'(z)})(\overline{\partial z/\partial s})\right)(\partial z/\partial s). \end{aligned} \tag{3.17}$$

3.2.3 Far-Field Boundary Condition Reformulation

The Goursat functions are used to reformulate the far-field boundary conditions given in (2.29), (2.30). The details are discussed in [14, 20, 24]. Note that by (2.30) as $z \to \infty$, the pressure tends to a constant. Using the definition of the function f, (3.2), and integrating with respect to z, an examination of the far-field behavior gives

$$f(z) \sim -\frac{i}{4}p_\infty(t)z + f_\infty(z) + B(t). \tag{3.18}$$

Here, p_∞ is determined as part of the solution and is discussed in a later section. $B(t)$ is an arbitrary function and is also discussed later, while $f_\infty(z)$ is discussed below.

Using the definition of velocity in terms of Goursat functions, (3.5), the far-field conditions for velocity, (2.29), and (3.18), another integration with respect to z and examination of the far-field behavior gives

$$g(z) \sim g_\infty(z) - \bar{B}(t). \tag{3.19}$$

The functions $f_\infty(z)$, $g_\infty(z)$ are chosen to satisfy the far-field velocity condition

$$f_\infty(z) + z\overline{f'_\infty(z)} + \overline{g'_\infty(z)} = i(u_\infty + iv_\infty), \tag{3.20}$$

where

$$u_\infty + iv_\infty = \frac{Q}{2}\left(\left(1 + i\frac{\beta_0}{\alpha_0}\right)\bar{z} + i\frac{\omega_0}{\alpha_0}z\right).$$

is obtained from (2.29).

Chapter 4

Integral Equation Reformulation

4.1 Fluid Problem

In order to determine the Goursat functions f and g subject to the reformulated boundary conditions discussed in the previous section, the functions are rewritten using *boundary integral representations*. In this case, the reformulated boundary conditions lead to integral equations that are solved to produce the Goursat functions. These integral equations are particularly amenable to numerical solution, as discussed in a later section. Further details regarding integral equations and representations are discussed in [20, 24, 26, 27].

The Goursat functions are rewritten in integral form by using the following representations [20, 26]

$$f(z) = \frac{1}{2\pi i}\int_{\partial\Omega}\frac{\gamma(\zeta)}{\zeta - z}d\zeta + \int_{\partial\Omega}\gamma(\zeta)ds - \frac{i}{4}p_\infty(t)z + f_\infty(z) + B(t), \tag{4.1}$$

$$g'(z) = \frac{1}{2\pi i}\int_{\partial\Omega}\frac{-\overline{\gamma(\zeta)}d\zeta + \gamma(\zeta)d\bar{\zeta}}{\zeta - z} - \frac{1}{2\pi i}\int_{\partial\Omega}\frac{\bar{\zeta}\gamma(\zeta)}{(\zeta - z)^2}d\zeta + g_\infty(z) - \bar{B}(t). \tag{4.2}$$

Here $\zeta, z \in \mathbb{C}$ with $\zeta \in \partial\Omega$. These representations contain *Cauchy-type* integrals. They are evaluated along the boundary, $\partial\Omega$, and as such are treated as *principal-value integrals*, since the kernels of the integrals are singular along the boundary. In addition, they are written in terms of an unknown complex density, $\gamma = \gamma(\zeta, t)$, which must be determined. This density function is only defined on the boundary $\partial\Omega$. As before, the time dependence of these functions is notationally suppressed $\gamma(\zeta) = \gamma(\zeta, t)$.

After substitution of (4.1), (4.2) into (3.16), use of the Plemelj formulae for evaluation of principal value integrals on contours, and simplification, the dynamic boundary condition

becomes the *Sherman-Lauricella* integral equation for γ

$$\begin{aligned}\gamma(z) &+ \frac{1}{2\pi i}\int_{\partial\Omega}\gamma(\zeta)\left(\frac{d\zeta}{\zeta - z} - \frac{d\bar{\zeta}}{\bar{\zeta} - \bar{z}}\right) + \frac{1}{2\pi i}\int_{\partial\Omega}\overline{\gamma(\zeta)}\left(\frac{d\zeta}{\bar{\zeta} - \bar{z}} - \frac{(z-\zeta)d\bar{\zeta}}{(\bar{\zeta} - \bar{z})^2}\right)\\ &+ \int_{\partial\Omega}\gamma(\zeta)ds = -\frac{\sigma}{2}\frac{\partial z}{\partial s} - \frac{i\beta}{4}\int_s\left(\frac{\partial\phi}{\partial n}\right)^2\frac{\partial z}{\partial s}ds + \frac{i}{2}p_\infty z\\ &- \left(f_\infty(z) - z\overline{f'_\infty(z)} - \overline{g'_\infty(z)}\right). \end{aligned} \tag{4.3}$$

In this case, the arbitrary function $B(t)$ is given as

$$B(t) = \frac{1}{2}\int_{\partial\Omega}\gamma(\zeta)ds,$$

and the far-field pressure $p_\infty(t)$ is chosen as

$$p_\infty(t) = -\frac{2}{\pi}\mathrm{Re}\left(\int_{\partial\Omega}\frac{\gamma(\zeta)}{(\zeta - z_c)^2}d\zeta\right).$$

This fixes a reference value for the pressure at z_c, which is an arbitrary point inside Ω_d [20].

As discussed in [24], (4.3) is a Fredholm integral equation of the second kind and is invertible for γ by the Fredholm alternative. In principle, once γ is determined from (4.3), it is used to update the velocity. Using (4.1) and (4.2) in (3.5), the velocity is determined from a boundary integral representation

$$u + iv = \frac{1}{2\pi i}\int_{\partial\Omega}\gamma(\zeta)\left(\frac{d\zeta}{\zeta - z} - \frac{d\bar{\zeta}}{\bar{\zeta} - \bar{z}}\right) + \frac{1}{2\pi i}\int_{\partial\Omega}\overline{\gamma(\zeta)}\left(\frac{d\zeta}{\bar{\zeta} - \bar{z}} - \frac{(z-\zeta)d\bar{\zeta}}{(\bar{\zeta} - \bar{z})^2}\right) + u_\infty + iv_\infty. \tag{4.4}$$

The velocity is then used in the kinematic boundary condition, (3.17), to advance the interface profile by calculating the points along the interface, z.

This completes the overview of the solution process for the fluid problem. The issue of solving the governing equations for the primitive variables in an infinite domain, subject to the appropriate boundary conditions is converted into the problem of determining appropriate complex potentials to satisfy given boundary conditions. This task, in turn, is completed by solving an integral equation along the interface of the bubble. In principle, the solution to this boundary integral equation exists. Once the solution is obtained, it is used to calculate the complex potentials. These potentials are used to determine the velocity, which, in turn, is used to calculate the location of the interface in time. However, in order to solve the boundary integral equation, the normal derivative of the electrostatic potential, $\partial\phi/\partial n$, is required. Once this quantity is calculated, the overall problem can be solved. Therefore, the discussion now shifts to the determination of the electrostatic potential and its normal derivative.

4.2 Electrostatic Boundary Value Problem

The electric potential, ϕ, is obtained by solving the electrostatic boundary value problem (2.24), which consists of Laplace's equation with Dirichlet boundary conditions. There are a number of well known analytical methods for solving this problem. In keeping with the theme of the previous section, the solution is formulated as a boundary integral representation. This approach to solving Laplace's equation is known as *potential theory* and is widely used [16, 18, 23, 29].

4.2.1 Boundary Integral Reformulation

The *fundamental solution*, Φ, to Laplace's equation, $\Delta u = 0$, in $\mathbb{R}^2$ is given by

$$\Phi(\mathbf{x}) = -\frac{1}{2\pi} \ln |\mathbf{x}|. \tag{4.5}$$

Here $|\mathbf{x}|$ represents the distance from the singularity at $\mathbf{x} = \mathbf{0}$. This solution, however, does not account for any boundary conditions associated with the equation. Given a region $\Gamma \subset \mathbb{R}^2$, it can be shown [12, 23] that any harmonic function, $u(\mathbf{x})$, $\mathbf{x} \in \Gamma$ has the following boundary integral representation

$$u(\mathbf{x}) = \int_{\partial\Gamma} \left[\Phi(\mathbf{y} - \mathbf{x}) \frac{\partial u}{\partial n_{\mathbf{y}}}(\mathbf{y}) - \frac{\partial \Phi}{\partial n_{\mathbf{y}}}(\mathbf{y} - \mathbf{x}) u(\mathbf{y}) \right] ds_{\mathbf{y}}. \tag{4.6}$$

Here $\partial / \partial n_{\mathbf{y}}$ represents the normal derivative with respect to $\mathbf{y} \in \partial\Gamma$ in the direction of the outward normal to Γ, and $ds_{\mathbf{y}}$ is the arclength differential used in an integration with respect to $\mathbf{y}$.

This integral representation is valid for any point $\mathbf{x} \in \Gamma$, but requires information about u and $\partial u / \partial n$ on the boundary $\partial\Gamma$. Unfortunately, in most boundary value problems, both these pieces of information are not known. For example, consider Laplace's equation in an unbounded region Γ external to a closed boundary $\partial\Gamma$, and subject to Dirichlet boundary conditions (this problem is analogous to the electrostatic boundary value problem discussed earlier)

$$\begin{cases} \Delta u = & 0, & \mathbf{x} \in \Gamma \\ u = & g, & \mathbf{x} \in \partial\Gamma. \end{cases} \tag{4.7}$$

For brevity, the far-field boundary condition is not included here. Clearly information about the normal derivative on the boundary $\partial\Gamma$ is unknown and (4.6) is not a useful representation of the solution. However, it is possible to obtain another boundary integral representation

for the Dirichlet problem. By way of introducing a *corrector function* H that satisfies the following boundary value problem:

$$\begin{cases} \Delta H = & 0, & \mathbf{x} \in \Gamma \\ H = & \Phi(\mathbf{y}-\mathbf{x}), & \mathbf{x}, \mathbf{y} \in \partial\Gamma, \end{cases}$$

and defining the *Green's function*

$$G(\mathbf{x}, \mathbf{y}) = \Phi(\mathbf{y}-\mathbf{x}) - H(\mathbf{y}), \tag{4.8}$$

it can be shown [12, 23] that the following boundary integral representation for the Dirichlet problem (4.7) is valid for any $\mathbf{x} \in \Gamma$

$$u(\mathbf{x}) = -\int_{\partial\Gamma} \frac{\partial G}{\partial n_{\mathbf{y}}}(\mathbf{x}, \mathbf{y}) g(\mathbf{y}) ds_{\mathbf{y}}. \tag{4.9}$$

Although (4.9) may appear to be an improvement, it is not of much practical use as it is extremely difficult to find explicit Green's functions other than for the most basic geometries. Once again, the boundary integral representation needs to be reformulated for use on a general boundary $\partial\Gamma$. However, (4.9) provides motivation for another useful representation.

The Green's function for the Laplacian operator, (4.8), is always comprised of the fundamental solution (4.5), and an additional harmonic corrector function. Therefore, the singularity of the Green's function is always of logarithmic form in $\mathbb{R}^2$, regardless of the geometry of the problem. This motivates an integral representation known as a *double-layer potential* [13, 23]:

$$\begin{aligned} u(\mathbf{x}) &= -\int_{\partial\Gamma} \frac{\partial \Phi}{\partial n_{\mathbf{y}}}(\mathbf{y}-\mathbf{x}) \mu(\mathbf{y}) ds_{\mathbf{y}} \\ &= \frac{1}{2\pi} \int_{\partial\Gamma} \frac{\partial}{\partial n_{\mathbf{y}}} \left(\ln |\mathbf{y}-\mathbf{x}|\right) \mu(\mathbf{y}) ds_{\mathbf{y}}. \end{aligned} \tag{4.10}$$

The double-layer potential is rewritten in complex form as

$$u(z) = \frac{1}{2\pi} \int_{\partial\Gamma} \mu(\zeta) \frac{\partial}{\partial n_\zeta} \left(\log |\zeta - z|\right) ds_\zeta, \text{ for } \zeta \in \partial\Gamma, z \in \Gamma. \tag{4.11}$$

Here $\zeta = \zeta(s)$ and log represents the magnitude of the complex logarithm function. It is equivalent to the real-valued natural logarithm, ln. The unknown function $\mu = \mu(\zeta)$ is a real-valued density function that plays a role similar to a charge density in electrostatics. Equation (4.10) has the same mathematical form as the potential induced by a double layer

of charges of opposite sign and density μ on a sheet $\partial\Gamma$ [13, 23], giving rise to the name double-layer potential.

The representation in (4.10) differs from (4.9) in that the normal derivative of the unknown Green's function has been replaced with the normal derivative of the fundamental solution. This is done in an attempt to simplify the expression yet maintain the behavior of the singularity of the Green's function. However, this is at the cost of introducing the unknown density function μ. Before using this type of representation, the answers to several questions are required:

- Does (4.10) represent a harmonic function?
- If so, does (4.10) satisfy Dirichlet boundary conditions?
- If so, does (4.10) produce a unique solution?
- How is the unknown function μ determined?

These questions are discussed in [23]. It turns out that if it is possible to find a function μ that is continuous on $\partial\Gamma$ such that

$$-\mu(z) + \frac{1}{\pi}\int_{\partial\Gamma} \mu(\zeta)\frac{\partial}{\partial n_\zeta}\left(\log|\zeta - z|\right) ds_\zeta = 2g(z), \text{ for all } \zeta, z \in \partial\Gamma, \tag{4.12}$$

then the double-layer potential, (4.11), solves Laplace's equation with Dirichlet boundary conditions, (4.7). Therefore, the solution to (4.7) depends on whether a solution, μ, to the integral equation in (4.12) exists. As proved in [13, 26], this equation is a *Fredholm integral equation of the second kind*, and is uniquely solvable for μ given any function g continuous on $\partial\Gamma$.

When solving the exterior Dirichlet problem, Γ is an unbounded region external to a boundary $\partial\Gamma$ and to produced a well-posed problem, (4.7) is supplemented by a far-field condition. In this case, the solution u is taken to be bounded at infinity. As a result of this condition, the double-layer potential is modified slightly. As discussed in [16, 26], it can be shown that the representation in (4.11) decays to zero in the far-field. To capture this possible bounded constant behavior, (4.11) is modified by adding a constant term

$$\begin{aligned} u(z) &= \frac{1}{2\pi}\int_{\partial\Gamma} \mu(\zeta)\frac{\partial}{\partial n_\zeta}\left(\log|\zeta - z|\right) ds_\zeta + \frac{1}{2\pi}\int_{\partial\Gamma}\mu(\zeta) ds_\zeta \\ &= \frac{1}{2\pi}\int_{\partial\Gamma} \mu(\zeta)\left[\frac{\partial}{\partial n_\zeta}\left(\log|\zeta - z|\right) + 1\right] ds_\zeta, \text{ for } \zeta \in \partial\Gamma, z \in \Gamma. \end{aligned} \tag{4.13}$$

In some cases, such as the modified electrostatic boundary value problem, (2.24), it may be true that the far-field behavior does in fact decay to zero, in which case the added contribution will be identically zero.

With this modification, the integral equation used to determine μ, (4.12), changes to

$$-\mu(z) + \frac{1}{\pi}\int_{\partial\Gamma}\left[\mu(\zeta)\frac{\partial}{\partial n_\zeta}\left(\log|\zeta - z|\right) + 1\right] ds_\zeta = 2g(z), \text{ for all } \zeta, z \in \partial\Gamma. \tag{4.14}$$

The above equation is also uniquely solvable for μ, as proved in [26].

Based on this discussion, the solution to the electrostatic problem, (2.24), is obtained by using boundary integral representations. The potential, ϕ, is represented in the external domain Ω as

$$\phi(z) = \frac{1}{2\pi}\int_{\partial\Omega}\mu(\zeta)\left[\frac{\partial}{\partial n_\zeta}\left(\log|\zeta - z|\right) + 1\right] ds_\zeta, \text{ for } \zeta \in \partial\Omega, z \in \Omega. \tag{4.15}$$

Using the boundary condition in (2.24), the unknown density μ is obtained by solving

$$-\mu(z) + \frac{1}{\pi}\int_{\partial\Omega}\left[\mu(\zeta)\frac{\partial}{\partial n_\zeta}\left(\log|\zeta - z|\right) + 1\right] ds_\zeta = 2\mathrm{Re}(z), \text{ for all } \zeta, z \in \partial\Omega. \tag{4.16}$$

4.2.2 Dirichlet-Neumann Map

The normal derivative of ϕ along the interface is required in the dynamic boundary condition, (4.3). Analytic function theory is used to evaluate this derivative. The electric potential is given by (4.15). This integral representation is the real part of an analytic function containing a Cauchy-type integral of the form

$$\Phi(z) = \frac{1}{2\pi i}\int_{\partial\Omega}\frac{\mu(\zeta)d\zeta}{\zeta - z} + \frac{1}{2\pi}\int_{\partial\Omega}\mu(\zeta)ds_\zeta. \tag{4.17}$$

Note that Φ is analytic for $\zeta \neq z$ (off of the integration contour). Since $d\zeta/(\zeta - z) = dr/r + id\theta$, where $r = |\zeta - z|$ and $\theta = \arg(\zeta - z)$, Φ is rewritten in terms of its real and imaginary parts

$$\begin{aligned}
\Phi &= \phi + i\psi \\
&= \frac{1}{2\pi}\int_{\partial\Omega}\mu(\zeta)d\theta - \frac{i}{2\pi}\int_{\partial\Omega}\mu(\zeta)\frac{dr}{r} + \frac{1}{2\pi}\int_{\partial\Omega}\mu(\zeta)ds_\zeta \\
&= \frac{1}{2\pi}\int_{\partial\Omega}\mu(\zeta)\frac{\partial}{\partial s_\zeta}\left(\arg|\zeta - z|\right)ds_\zeta - \frac{i}{2\pi}\int_{\partial\Omega}\mu(\zeta)\frac{\partial}{\partial s_\zeta}\left(\log|\zeta - z|\right)ds_\zeta \\
&\quad + \frac{1}{2\pi}\int_{\partial\Omega}\mu(\zeta)ds_\zeta.
\end{aligned} \tag{4.18}$$

Here $\partial/\partial s_\zeta$ is the tangential derivative with respect to the variable ζ. Noting that $\log(\zeta - z)$ is an analytic function for $\zeta \neq z$ (off of $\partial\Omega$), the Cauchy-Riemann equations

$$\begin{aligned} \frac{\partial}{\partial s}\left(\log|\zeta - z|\right) &= -\frac{\partial}{\partial n}\left(\arg(\zeta - z)\right), \\ \frac{\partial}{\partial n}\left(\log|\zeta - z|\right) &= \frac{\partial}{\partial s}\left(\arg(\zeta - z)\right), \end{aligned}$$

are used to rewrite the integrand of the real component of (4.18) as

$$\Phi = \frac{1}{2\pi}\int_{\partial\Omega}\mu(\zeta)\left[\frac{\partial}{\partial n_\zeta}\left(\log|\zeta - z|\right) + 1\right] ds_\zeta - \frac{i}{2\pi}\int_{\partial\Omega}\mu(\zeta)\frac{\partial}{\partial s_\zeta}\left(\log|\zeta - z|\right) ds_\zeta. \tag{4.19}$$

Here, $\phi = \mathrm{Re}(\Phi)$ is the integral representation (4.15) used for solving the Dirichlet problem (2.24). The form of the imaginary component is

$$\psi = \mathrm{Im}(\Phi) = -\frac{1}{2\pi}\int_{\partial\Omega}\mu(\zeta)\frac{\partial}{\partial s_\zeta}\left(\log|\zeta - z|\right) ds_\zeta. \tag{4.20}$$

Since the function $\Phi = \phi + i\psi$ is analytic, by the above Cauchy-Riemann conditions $\partial\phi/\partial n = \partial\psi/\partial s$. Therefore, the normal component of the potential along the interface is found by computing the tangential derivative of the harmonic conjugate ψ along the interface. Once the tangential derivative is calculated, it is used in the electric stress term in the dynamic boundary condition, (2.26) to couple the electrostatic problem to the fluid dynamical problem. The electrohydrodynamic problem is now fully represented in boundary integral form.

Chapter 5

Numerical Methods

The coupled fluid-electric free boundary problem discussed in earlier sections is reformulated using integral equations, which are in turn solved using numerical methods. In particular, the fast multipole method is used in conjunction with an iterative solver to rapidly solve the integral equations given in (4.3) and (4.16). The process is described below.

5.1 Numerical Stokes Flow Solver

An existing computer program written in Fortran77 is used to solve a variety of Stokes flow problems that do not include electrostatic effects [14, 20, 24]. The electrostatic problem is solved by supplementing the program with appropriate numerical routines. Since the electrostatic solver is housed within this existing program, the numerical implementation of the Stokes flow solver is briefly described below. The implementation is discussed in greater detail within [20, 24].

5.1.1 Equal Arclength Parameterization

The problem is first reformulated in the *equal arclength frame*. As discussed in [17, 20, 24], the interface profile is determined solely by the normal component of the velocity, as seen from the kinematic boundary condition

$$\frac{d\mathbf{x}}{dt} = (\mathbf{u} \cdot \mathbf{n})\mathbf{n}.$$

Numerically, the grid points making up the interface are advected by the flow and tend to cluster in regions of high curvature. In turn, this leads to an inadequate interface resolution

and affects the time-stepping stability constraint, as $\Delta t = \mathcal{O}(\min(\Delta s_i))$, where Δs_i represents the non-uniform spacing of the interface grid points. To counteract this clustering effect, a tangential component is added to the kinematic boundary condition

$$\frac{d\mathbf{x}}{dt} = (\mathbf{u}\cdot\mathbf{n})\mathbf{n} + T\mathbf{s}. \tag{5.1}$$

This tangential component T has no effect on the interface location. However, if chosen correctly, it prevents clustering along the interface by implementing an equal arclength spacing, Δs, between grid points, thus maintaining a uniform $\Delta t = \mathcal{O}(\Delta s)$ condition.

The equal arclength frame is achieved initially by using Newton's method to solve a set of non-linear algebraic equations for the locations of the equally spaced grid points along the interface. The tangential component T is computed at every time step from the velocity on the boundary $\partial\Omega$. Further details are provided in [17]. The equi-spaced locations are embedded into other aspects of the problem through a reparameterization. Using a parameter $\alpha \in [0, 2\pi)$, points along the interface are assigned to equally spaced parameter values, $\alpha_j = \frac{2\pi}{N} j,\ 1 \le j \le N$, where N is the number of grid points along the interface. These equally spaced points are given in $\mathbb{C}$ by $z(\alpha, t) = x(\alpha, t) + iy(\alpha, t)$. The arclength along the interface is also given in terms of this parameter, $s = s(\alpha, t)$ and $\partial s/\partial\alpha$ is a function of time only.

The Sherman-Lauricella integral equation representing the dynamic boundary condition, (4.3), is parameterized in terms of α. The unknown density is written as a function of the new parameter, $\gamma(\zeta, t) = \gamma(\zeta(\alpha), t) = \gamma(\alpha, t)$

$$\begin{aligned}
\gamma(\alpha) &+ \int_0^{2\pi} \gamma(\nu) K_1(z(\alpha), z(\nu))\, d\nu + \int_0^{2\pi} \overline{\gamma(\nu)} K_2(z(\alpha), z(\nu))\, d\nu \\
&+ \int_0^{2\pi} \gamma(\nu) \frac{\partial s}{\partial \nu} d\nu = -\frac{\sigma}{2} \frac{\partial z}{\partial \alpha} \Big/ \frac{\partial s}{\partial \alpha} - \frac{i\beta}{4} \int_\alpha \left(\frac{\partial \phi}{\partial n} \right)^2 \frac{\partial z}{\partial \alpha} d\alpha + \frac{i}{2} p_\infty z(\alpha) \\
&- \left(f_\infty(z(\alpha)) - z(\alpha) \overline{f'_\infty(z(\alpha))} - \overline{g'_\infty(z(\alpha))} \right).
\end{aligned} \tag{5.2}$$

As before, the time dependence of the functions is notationally suppressed, $\gamma(\alpha, t) = \gamma(\alpha)$. The kernels K_1, K_2 are given by

$$K_1(z(\alpha), z(\nu)) = \frac{1}{2\pi i} \left(\frac{\partial z/\partial \nu(\nu)}{z(\nu) - z(\alpha)} - \frac{\overline{\partial z/\partial \nu}(\nu)}{\overline{z}(\nu) - \overline{z}(\alpha)} \right), \tag{5.3}$$

$$K_2(z(\alpha), z(\nu)) = \frac{1}{2\pi i} \left(\frac{\partial z/\partial \nu(\nu)}{\overline{z}(\nu) - \overline{z}(\alpha)} - \frac{(z(\nu) - z(\alpha))\overline{\partial z/\partial \nu}(\nu)}{(\overline{z(\nu)} - \overline{z(\alpha)})^2} \right). \tag{5.4}$$

The velocity, (4.4), is given by

$$u + iv = \int_0^{2\pi} \gamma(\nu) K_1'(z(\alpha), z(\nu)) d\nu + i \int_0^{2\pi} \overline{\gamma(\nu)} K_2(z(\alpha), z(\nu)) d\nu + u_\infty + i v_\infty, \tag{5.5}$$

where K_2 is as in (5.4) and K_1' is given by

$$K_1'(z(\alpha), z(\nu)) = \frac{1}{2\pi} \left(\frac{\partial z / \partial \nu(\nu)}{z(\nu) - z(\alpha)} + \frac{\overline{\partial z / \partial \nu}(\nu)}{\overline{z}(\nu) - \overline{z}(\alpha)} \right). \tag{5.6}$$

Any applicable terms in the electrostatic problem are also reformulated in the equal arclength frame. The electric stress term in (5.2) is represented by the following equivalent forms

$$\begin{aligned} -\frac{i\beta}{4} \int_s \left(\frac{\partial \phi}{\partial n} \right)^2 \frac{\partial z}{\partial s} ds &= -\frac{i\beta}{4} \int_z \left(\frac{\partial \phi}{\partial n} \right)^2 dz \\ &= -\frac{i\beta}{4} \int_\alpha \left(\frac{\partial \phi}{\partial n} \right)^2 \frac{\partial z}{\partial \alpha} d\alpha. \end{aligned}$$

As discussed in the previous section, the normal derivative of the electric potential is obtained from the tangential derivative of the harmonic conjugate. This derivative is also reparameterized with respect to α and written as

$$\frac{\partial \psi}{\partial s} = \frac{\partial \psi}{\partial \alpha} / \frac{\partial s}{\partial \alpha}. \tag{5.7}$$

5.1.2 Spectral Discretization

Since the interface is a closed curve, it is treated as a 2π-periodic domain and is amenable to a spectral description. As discussed above, the interface is partitioned into N grid points, equally spaced in both arclength and α. Here $\alpha_j = \frac{2\pi}{N} j$, $1 \le j \le N$ represents the parameter value for the jth grid point along the interface, given by $z(\alpha_j) = z_j = x_j + i y_j$. Similarly, for any function, $f(\alpha_j) = f_j$. Discrete Fourier transforms (DFT) are applied to functions along the interface to achieve spectral accuracy. In particular, the DFT and inverse DFT (IDFT) are used

$$\hat{f}_k = \sum_{j=1}^{N} f_j e^{-ik\alpha_j}, \quad \text{for } k = -\tfrac{N}{2} + 1, \ldots, \tfrac{N}{2},$$

$$f_j = \frac{1}{N} \sum_{k=-N/2+1}^{N/2} \hat{f}_k e^{ik\alpha_j}, \quad \text{for } j = 1, \ldots, N.$$

In addition, N is a power of two so that the fast Fourier transform (FFT) is used to compute the DFT and the IDFT. Using the FFT, differentiation and integration of functions are performed easily, and to spectral accuracy, in Fourier space

$$\begin{aligned}\frac{d^n}{dx^n}(f_j) &= \frac{1}{N}\sum_{k=-N/2+1}^{N/2}(ik)^n\hat{f}_k e^{ik\alpha_j}, \quad \text{for } j=1,\ldots,N,\\ \int_0^{\alpha_j} f(\alpha_j)d\alpha &= \hat{f}_0\alpha_j + \sum_{k=-N/2+1,k\neq 0}^{N/2}\frac{\hat{f}_k}{ik}e^{ik\alpha_j}, \quad \text{for } j=1,\ldots,N.\end{aligned}$$

These transforms are applied to spatial variables only. The time behavior of the functions is not computed spectrally, but instead with standard numerical techniques discussed briefly in a later section.

5.1.3 Numerical Solution of Integral Equations

The main numerical issue in the Stokes solver is the solution of the integral equation, (5.2). The integrals in (5.2) are discretized using the *trapezoidal rule*, which maintains spectral accuracy on sufficiently smooth boundaries [20, 34]. Using a grid spacing of $h = 2\pi/N$, the discretized form of (5.2) is

$$\begin{aligned}\gamma_j &+ \sum_{i=1}^{N}K_1(z_j,z_i)\gamma_i + \sum_{i=1}^{N}K_2(z_j,z_i)\overline{\gamma_i} + h\sum_{i=1}^{N}\gamma_i\left(\frac{\partial s}{\partial\alpha}\right)_i\\ &+ i\frac{h}{2\pi}z_j\sum_{i=1}^{N}\mathrm{Re}\left(\frac{\gamma_i\left(\partial z/\partial\alpha\right)_i}{(z_i-z_c)^2}\right) = g_j,\end{aligned} \tag{5.8}$$

with

$$g_j = -\frac{\sigma_j}{2}\frac{\left(\partial s/\partial\alpha\right)_j}{\left|\left(\partial s/\partial\alpha\right)_j\right|} - \frac{i\beta}{4}\left(\int_\alpha\left(\frac{\partial\phi}{\partial n}\right)^2\frac{\partial z}{\partial\alpha}d\alpha\right)_j - \left(f_\infty(z_j) - z_j\overline{f'_\infty(z_j)} - \overline{g'_\infty(z_j)}\right). \tag{5.9}$$

The integration in the electric stress term is performed with the Fourier integration method described earlier. Discussion regarding the numerical computation of $\partial\phi/\partial n$ is deferred to a later section. The discretized form of the kernels, K_1, K_2, are

$$\begin{aligned}K_1(z_j,z_i) &= \frac{h}{2\pi i}\left(\frac{\left(\partial z/\partial\alpha\right)_i}{z_i-z_j} - \frac{\overline{\left(\partial z/\partial\alpha\right)_i}}{\overline{z_i}-\overline{z_j}}\right),\\ K_2(z_j,z_i) &= \frac{h}{2\pi i}\left(\frac{\left(\partial z/\partial\alpha\right)_i}{\overline{z_i}-\overline{z_j}} - \frac{(z_i-z_j)\overline{\left(\partial z/\partial\alpha\right)_i}}{(\overline{z_i}-\overline{z_j})^2}\right).\end{aligned}$$

Note that the kernels are singular for $z_i = z_j$. However, in this case, it can be shown [20] using Taylor series expansions that the kernels have a continuous limit in terms of the curvature, κ, of the interface

$$\begin{aligned} K_1(z_j, z_j) &= \frac{h}{2\pi}\kappa_j |(\partial z/\partial\alpha)_j|, \\ K_2(z_j, z_j) &= \frac{h}{2\pi}\kappa_j \frac{(\partial z/\partial\alpha)_j^2}{|(\partial z/\partial\alpha)_j|}. \end{aligned}$$

The curvature is calculated pseudo-spectrally using Fourier differentiation

$$\kappa_j = \frac{(\partial x/\partial\alpha)(\partial^2 y/\partial\alpha^2) - (\partial y/\partial\alpha)(\partial^2 x/\partial\alpha^2)}{((\partial x/\partial\alpha)^2 + (\partial y/\partial\alpha)^2)^{3/2}}.$$

Using the above discretization leads to a linear system of equations of the form

$$\left(\mathbf{I} + \mathbf{K_1} + \overline{\mathbf{K_2}} + \mathbf{M_1} + \mathbf{M_2}\right)\boldsymbol{\gamma} = \mathbf{g}. \tag{5.10}$$

Here I is the $N \times N$ identity matrix, $\mathbf{K_1}, \mathbf{K_2}$, $\mathbf{M_1}$, and $\mathbf{M_2}$ are $N \times N$ matrices, with entries given by

$$\begin{aligned} \mathbf{K_1}_{ij} &= K_1(z_j, z_i), \\ \overline{\mathbf{K_2}}_{ij} &= \overline{K_2(z_j, z_i)}, \\ \mathbf{M_1}_{ij} &= h(\partial s/\partial\alpha), \\ \mathbf{M_2}_{ij} &= \tfrac{ihz_j}{2\pi}\mathrm{Re}\left((\partial z/\partial\alpha)_i/(z_i - z_c)^2\right). \end{aligned}$$

Note that each of these matrices is dense. In addition, $\boldsymbol{\gamma} = (\gamma_1, \ldots, \gamma_N)$ is the vector of unknowns, and $\mathbf{g} = (g_1, \ldots, g_N)$ is obtained from evaluation of (5.9) at grid points along the interface.

The system, (5.10), is solved iteratively using the *generalized minimum residual method* (GMRES). Since (5.10) is obtained from a Fredholm integral equation of the second kind, GMRES solves this system in a fixed number of iterations, independent of the system size N [20, 35]. The floating point operation (flop) cost per iteration is $\mathcal{O}(N^2)$, with the majority of the computational working coming from a required matrix-vector multiplication. While this offers a significant savings over the $\mathcal{O}(N^3)$ flop count required for direct solution methods such as Gaussian elimination, it is still computationally expensive to solve this linear system using GMRES directly. In addition, when using GMRES, the matrix is stored in computational memory at a storage cost of $\mathcal{O}(N^2)$ bytes. Although an improvement over

direct methods, this operation count and storage requirement is prohibitive when solving systems with large N ($\geq 10^4$).

The iterative procedure is accelerated by using the *fast multipole method* (FMM) [6] to compute the matrix-vector product in (5.10) in $\mathcal{O}(N)$ flops. FMM uses the structure of the dense matrices in (5.10) to quickly and efficiently compute the matrix-vector product required in GMRES. When using the FMM, the matrix is never explicitly calculated or stored in memory, offering a significant savings in both storage requirements and computational cost.

Once (5.10) is solved for γ, it is used in (5.5) to update the velocity. As in (5.2), the expression is discretized using the trapezoidal rule to preserve spectral accuracy

$$(u+iv)_j = \sum_{i=1}^{N} K_1'(z_j, z_i)\gamma_i + i\sum_{i=1}^{N} K_2(z_j, z_i)\overline{\gamma_i} + (u_\infty + iv_\infty)_j.$$

This results in another matrix-vector product of the form

$$\mathbf{u} + \mathbf{iv} = (\mathbf{K_1'} + \overline{\mathbf{K_2}})\boldsymbol{\gamma} + (\mathbf{u}_\infty + \mathbf{iv}_\infty). \tag{5.11}$$

Here $\mathbf{K_2}$ is the matrix defined in (5.10), and $\mathbf{K_1'}$ is defined based on (5.6)

$$K_1'(z_j, z_i) = -\frac{h}{2\pi}\left(\frac{(\partial z/\partial\alpha)_i}{z_i - z_j} + \frac{\overline{(\partial z/\partial\alpha)_i}}{\overline{z_i} - \overline{z_j}}\right). \tag{5.12}$$

The singular limit of (5.12) is

$$K_1'(z_j, z_j) = -\frac{h}{2\pi}\mathrm{Re}\left(\frac{(\partial^2 z/\partial\alpha^2)_j}{(\partial z/\partial\alpha)_j}\right).$$

As discussed in [20], the FMM is used to compute the matrix-vector product in (5.11) in an $\mathcal{O}(N)$ flop count.

5.1.4 Time Discretization

Once the velocity is obtained from the representation in (5.11), the interface location is updated in time. The modified kinematic boundary condition, (5.1) is discretized in time using an explicit midpoint second-order Runge-Kutta method. The interface grid points are evolved in time accordingly. All details are discussed in [20, 24].

5.2 Numerical Electrostatic Solver

5.2.1 Discretization of Integral Equation

The electrostatic potential, ϕ, is obtained from the integral representation, (4.15). The unknown density function, μ, is required in this representation. The integral equation in (4.16) is numerically solved for μ, and the potential is reconstructed using computed μ values. To maintain spectral accuracy, (4.16) is discretized using the trapezoidal rule with N grid points spaced equally in arclength along the boundary $\partial\Omega$. The integrals are then represented as summations over all grid points along the interface. The discrete form of (4.16) is

$$-\mu_i + \frac{h}{\pi}\sum_{j=1}^{N}\mu_j\left[\frac{\partial}{\partial n_j}\left(\log|z_j - z_i|\right) + 1\right] = 2\mathrm{Re}(z_i). \tag{5.13}$$

Here h is the arclength between nodes. As before, the boundary $\partial\Omega$ is described parametrically by $z(\alpha) = x(\alpha) + iy(\alpha)$. The normal derivative is rewritten by noting that $\frac{\partial}{\partial n} = \mathbf{n}\cdot\nabla$ and $|z_j - z_i| = \sqrt{(x_j - x_i)^2 + (y_j - y_i)^2} = \sqrt{(\Delta x_j)^2 + (\Delta y_j)^2}$. Writing $\mathbf{n} = n_x\hat{\mathbf{i}} + n_y\hat{\mathbf{j}}$, (5.13) becomes

$$-\mu_i + \frac{h}{\pi}\sum_{j=1}^{N}\mu_j\left[\frac{n_{x_j}\Delta x_j + n_{y_j}\Delta y_j}{(\Delta x_j)^2 + (\Delta y_j)^2} + 1\right] = 2\mathrm{Re}(z_i). \tag{5.14}$$

This equation is valid for $i \neq j$. In the case where $i = j$, the normal derivative of the logarithmic term is equal to half the curvature at z_i, $\kappa_i = \kappa(z_i)$, as $z_j \to z_i$, [36] as shown by a Taylor series expansion of the terms within the expression

$$\frac{\partial}{\partial n_j}\left(\log|z_j - z_i|\right) = \frac{1}{2}\frac{|\dot{x}\ddot{y} - \dot{y}\ddot{x}|}{[(\dot{x})^2 + (\dot{y})^2]^{3/2}} = \kappa_i, \text{ as } z_j \to z_i. \tag{5.15}$$

Letting

$$\alpha_j = \frac{n_{x_j}\Delta x_j + n_{y_j}\Delta y_j}{(\Delta x_j)^2 + (\Delta y_j)^2},$$

and expanding the summation in (5.14) gives the following equation at the i-th node

$$\frac{h}{\pi}\left[(\alpha_1 + 1)\mu_1 + (\alpha_2 + 1)\mu_2 + \ldots + \left(-\frac{\pi}{h} + \left(\frac{\kappa_i}{2} + 1\right)\right)\mu_i + \ldots + (\alpha_N + 1)\mu_N\right] = 2\mathrm{Re}(z_i).$$

Repeating this process for each node gives a linear system of N equations for the densities of the form

$$(\mathbf{I} - \boldsymbol{\kappa} - \mathbf{C} - \mathrm{Re}(\mathbf{H}))\boldsymbol{\mu} = -2\mathbf{g}. \tag{5.16}$$

Here, $\mathbf{I}$ is the $N \times N$ identity matrix, $\boldsymbol{\kappa}$ is an $N \times N$ diagonal matrix with the curvature values on the diagonal:

$$\boldsymbol{\kappa} = \frac{1}{2} \begin{pmatrix} \kappa_1 & 0 & \dots & 0 \\ 0 & \kappa_2 & \dots & 0 \\ 0 & 0 & \ddots & 0 \\ 0 & 0 & \dots & \kappa_N \end{pmatrix},$$

$\mathbf{C}$ is an $N \times N$ constant matrix:

$$\mathbf{C} = \frac{h}{\pi} \begin{pmatrix} 1 & 1 & \dots & 1 \\ 1 & 1 & \dots & 1 \\ \vdots & \vdots & \vdots & \vdots \\ 1 & 1 & \dots & 1 \end{pmatrix},$$

and $\mathbf{H}$ is an $N \times N$ *Hilbert matrix* [6] of the form:

$$\mathbf{H} = -\frac{1}{\pi i} \begin{pmatrix} 0 & \frac{1}{z_1 - z_2} & \dots & \dots & \frac{1}{z_1 - z_N} \\ \frac{1}{z_2 - z_1} & 0 & \dots & \dots & \frac{1}{z_2 - z_N} \\ \vdots & \vdots & \ddots & \vdots & \vdots \\ \frac{1}{z_j - z_1} & \dots & 0 & \dots & \frac{1}{z_j - z_N} \\ \vdots & \vdots & \ddots & \vdots & \vdots \\ \frac{1}{z_N - z_1} & \frac{1}{z_N - z_2} & \dots & \dots & 0 \end{pmatrix},$$

The Hilbert matrix has zeros along the main diagonal and non-zero entries of the form $\mathbf{H}_{ij} = \frac{1}{z_i - z_j}$, $i \neq j$. In addition, $\boldsymbol{\mu} = (\mu_1, \dots, \mu_N)$ is the vector of discrete unknown density values, while $\mathbf{g} = (g_1, \dots, g_N)$ is the vector of discrete values of the right-hand side of (5.13).

The system (5.16) is solved iteratively using GMRES accelerated by the FMM. The FMM is used to compute only the matrix-vector product $\mathbf{H}\boldsymbol{\mu}$ in (5.16), as all the other matrix-vector products are trivial and are obtained without explicit multiplication. As with the Stokes solver, the matrices are neither explicitly calculated or stored in computational memory. The result is a method that solves the Laplace problem in an $\mathcal{O}(N)$ flop count. Once the densities μ_i are determined, the solution $\phi_i = \phi(z_i)$ is reconstructed using a discrete integral representation

$$\phi_i = \frac{h}{2\pi} \sum_{j=1}^{N} \mu_j \left[\frac{\partial}{\partial n_j} \left(\log |z_j - z_i| \right) + 1 \right]. \tag{5.17}$$

When discretized with the trapezoidal rule, this representation has the following matrix-vector product form and results in a vector of discretized values for the potential, $\boldsymbol{\phi} = (\phi_1, \phi_2, \ldots, \phi_N)$

$$\boldsymbol{\phi} = (\mathbf{K} + \tfrac{1}{2}\mathbf{C})\boldsymbol{\mu}. \tag{5.18}$$

Once again, the matrix-vector product $\mathbf{C}\boldsymbol{\mu}$ is trivial to compute, and the product $\mathbf{K}\boldsymbol{\mu}$ is computed via the FMM. As before, the matrices in (5.18) are neither calculated or stored in memory.

5.2.2 Discretization of Harmonic Conjugate

Once the discrete values of the potential are obtained from (5.18), they are used to compute the values of the harmonic conjugate, ψ_i, along the interface. This term is subsequently used in the computation of the tangential derivative, $\partial\psi/\partial s$. As discussed in an earlier section, by the Cauchy-Riemann equations, this term is equal to the normal derivative of the potential, needed for the dynamic boundary condition (4.3).

Using the analytic function Φ from (4.19), the integral representation for ψ is given by (4.20). However, Φ contains a Cauchy-type integral and instead of discretizing (4.20) explicitly, the FMM is once again used to evaluate the principal-value integral in (4.19). The integral is recast into parametric form with respect to α

$$\frac{1}{2\pi i}\int_{\partial\Omega}\frac{\mu(\zeta)d\zeta}{\zeta - z} = \frac{1}{2\pi i}\int_{\partial\Omega}\frac{\mu(\alpha)\frac{\partial\zeta}{\partial\alpha}d\alpha}{\zeta(\alpha) - z}. \tag{5.19}$$

Using the trapezoidal rule in an equi-spaced arclength discretization, (5.19) has the following discrete form

$$\Phi_k = (\phi + i\psi)_k = \frac{h}{2\pi i}\sum_{j=1}^{N}\frac{\mu_j\left(\partial\zeta/\partial\alpha\right)_j}{\zeta_j - z_k}. \tag{5.20}$$

As mentioned, (5.20) is singular on $\partial\Omega$. Unlike in the case of the potential ϕ in (5.15), there is no convenient representation that allows the singular limit to be replaced with a continuous function. Therefore, another approach is adopted for this calculation. The *alternating point trapezoidal method* is used to calculate the integral value along the interface [25]. Essentially, the interface mesh is divided up into odd and even points. For an equi-arclength spacing, the value of the integral at odd grid points is calculated by using the above discretization at even points and vice versa. This avoids the singularity and still achieves spectral accuracy in computations. The alternating point trapezoidal method is efficiently computed by the

FMM, as the kernel is an expression of the form $\frac{1}{\zeta - z}$ [6]. Once this is calculated, the imaginary part of the expression is extracted, and its tangential derivative is found using Fourier differentiation. The resulting term is used in the dynamic boundary condition (4.3).

5.3 Test Cases

The Stokes solver has been tested in various capacities and its correctness verified and documented [14, 20, 24]. The Laplace solver is a new addition to the program and its correctness is verified using a series of numerical test cases described below.

5.3.1 Test Case - Calculation of Potential

The Laplace solver is tested against the known solution of an exterior Dirichlet problem [4]. The integral equation (4.16) is solved in an unbounded domain Γ exterior to the ellipse $\partial\Gamma : \mathbf{R}(t) = (a\cos t, b\sin t)$, $t \in [0, 2\pi]$:

$$\begin{cases} \Delta u &= 0, & \mathbf{x} \in \Gamma \\ u &= e^{\frac{x}{x^2+y^2}} \cos\left(\dfrac{y}{x^2+y^2}\right), & \mathbf{x} \in \partial\Gamma. \end{cases} \tag{5.21}$$

In this test, two sets of values for a and b are used, namely $a = 1, b = 2$ and $a = 1, b = 5$. The solution is computed along a row of points exterior to the ellipse, $\mathbf{c}(\theta) = q(\cos\theta, \sin\theta)$, where q takes on values $q > \frac{3}{2}$, and θ is the angle of the ray with respect to the x-axis. Each case has $\theta = \frac{4\pi}{3}$. The geometry and test points are illustrated in Figure 5.1 and Figure 5.2.

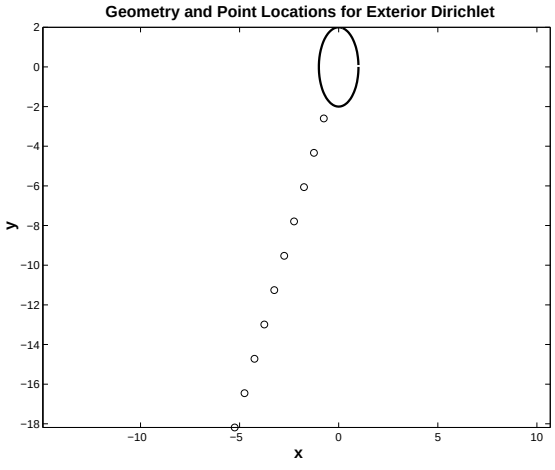

Figure 5.1: Geometry for Exterior Dirichlet Problem, $a = 1, b = 2$

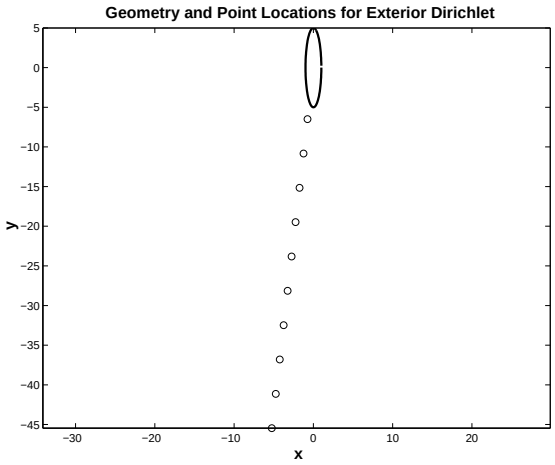

Figure 5.2: Geometry for Exterior Dirichlet Problem, $a = 1, b = 5$

The exact solution to the problem is

$$u_e(x, y) = e^{\frac{x}{x^2+y^2}} \cos\left(\frac{y}{x^2+y^2}\right). \tag{5.22}$$

A grid convergence study is performed to assess the convergence of the method to the exact solution. The infinity norm, $L_\infty = \max_{1 \le i \le N} |u_i - u_e|$, is used to compute the error between the computed solution u and the exact solution given in (5.22). The error tolerance for both the GMRES and FMM are set to 10^{-13}. The results are given in the tables and figures below.

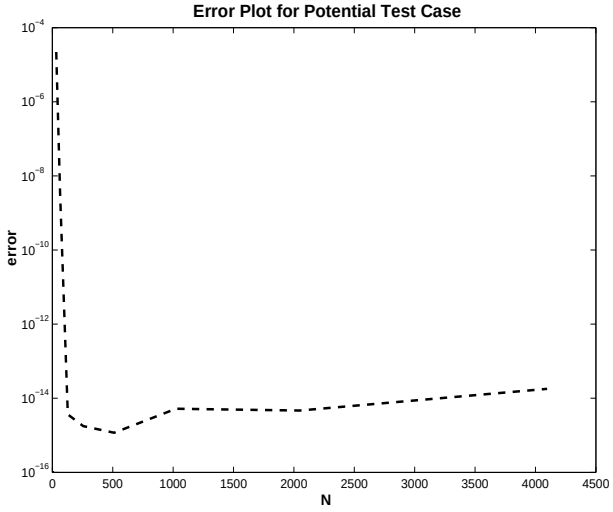

Figure 5.3: Errors for Potential Test Case, $a = 1, b = 2$

N	32	64	128	256	512	1024	2048	4096
L_∞	2.21e-5	3.37e-9	3.66e-15	1.78e-15	1.18e-15	5.22e-15	4.66e-15	1.80e-14
Ratio	-	6.54e3	9.20e5	2.06	1.51	0.23	1.12	0.26

Table 5.1: Errors for Potential Test Case, $a = 1$, $b = 2$

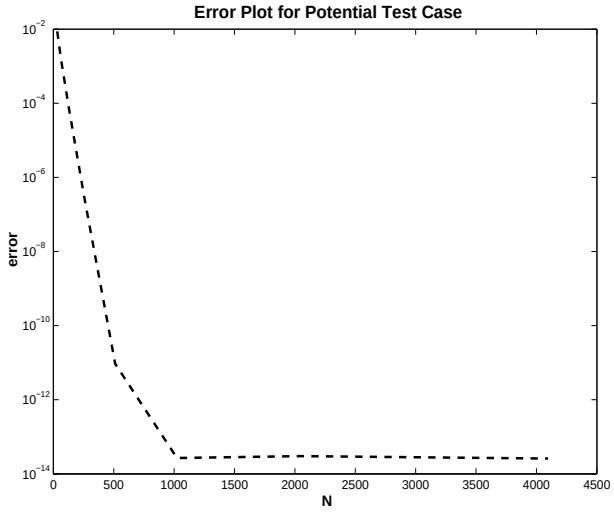

Figure 5.4: Errors for Potential Test Case, $a = 1, b = 5$

N	32	64	128	256	512	1024	2048	4096
L_∞	8.68e-3	1.49e-3	7.60e-5	2.96e-7	9.306e-12	2.68e-14	3.02e-14	2.60e-14
Ratio	-	5.81	19.64	256.64	31,866	347.50	0.89	1.16

Table 5.2: Errors for Potential Test Case, $a = 1, b = 5$

Both cases converge to the exact result with spectral accuracy, as evidenced by the ratios of the error norms in Table 5.1 and Table 5.2, and by the plots of the error norms in Figure 5.3 and Figure 5.4. The convergence to machine error is slower for the ellipse with higher eccentricity. This is an expected result due to the increased deformation in the ellipse. The above results suggest a successful implementation of the Laplace solver for the exterior Dirichlet problem.

5.3.2 Test Case - Principal Value Integrals and Derivative of Harmonic Conjugate

The implementation of the alternating point trapezoidal method for the Cauchy-type integrals used in the calculation of the harmonic conjugate of the electric potential is investigated using test cases. As discussed earlier, the harmonic conjugate of the potential is given by

$$\begin{aligned}\psi &= \mathrm{Im}(\Phi) \\ &= \mathrm{Im}\left(\frac{1}{2\pi i}\int_{\partial\Omega}\frac{\mu(\zeta)d\zeta}{\zeta - z} + \frac{1}{2\pi}\int_{\partial\Omega}\mu(\zeta)ds_\zeta\right) \\ &= \mathrm{Im}\left(\frac{1}{2\pi i}\int_{\partial\Omega}\frac{\mu(\zeta)d\zeta}{\zeta - z}\right).\end{aligned}$$

To evaluate this expression, each test case makes use of the Plemelj formulae [1] for evaluating a principal value integral along a closed contour C

$$\chi^{\pm}(t) = \pm\frac{\varphi(t)}{2} + \frac{1}{2\pi i}\int_C \frac{\varphi(\tau)}{t-\tau}d\tau. \tag{5.23}$$

Here the $\pm$ refers to the approach of a point on the contour from either the exterior $(-)$ or interior $(+)$ of the curve C, respectively. $\chi^{\pm}$ is a sectionally analytic function in either the interior or exterior, found by evaluating the integral away from the contour in the corresponding region. This function is computed with complex contour integration, and is used to rearrange (5.23) for the principal value integral on the contour itself. From above, the harmonic conjugate ψ is the imaginary component of this integral. Fourier differentiation is used to obtain the tangential derivative $\partial\psi/\partial s = (\partial\psi/\partial\alpha)/(\partial s/\partial\alpha)$.

For this test problem, $\varphi(\tau) = \tau + \frac{1}{\tau}$, along the contour $C : \frac{x^2}{9} + y^2 = 1$, giving

$$\frac{1}{2\pi i}\int_C \frac{\varphi(\tau)}{t-\tau}d\tau = \frac{1}{2}\left(t - \frac{1}{t}\right).$$

Here the exact harmonic conjugate is

$$\psi_e = \mathrm{Im}\left(\frac{1}{2}\left(t - \frac{1}{t}\right)\right) = \frac{y}{2}\left(1 + \frac{1}{x^2+y^2}\right).$$

The exact tangential derivative is given by

$$\begin{aligned}\left(\frac{\partial\psi}{\partial s}\right)_e &= \mathbf{s}\cdot\nabla\psi \\ &= s_x\frac{\partial\psi}{\partial x} + s_y\frac{\partial\psi}{\partial y} \\ &= s_x\left(-\frac{xy}{(x^2+y^2)^2}\right) + s_y\left(\frac{1}{2}\left(1 + \frac{1}{x^2+y^2}\right) - \frac{y^2}{(x^2+y^2)^2}\right).\end{aligned}$$

The components of the tangent vector are computed by the code for the particular choice of geometry. The error L_∞ is computed by taking the maximum magnitude of the difference between the computed and exact solutions for both the harmonic conjugate and its derivative.

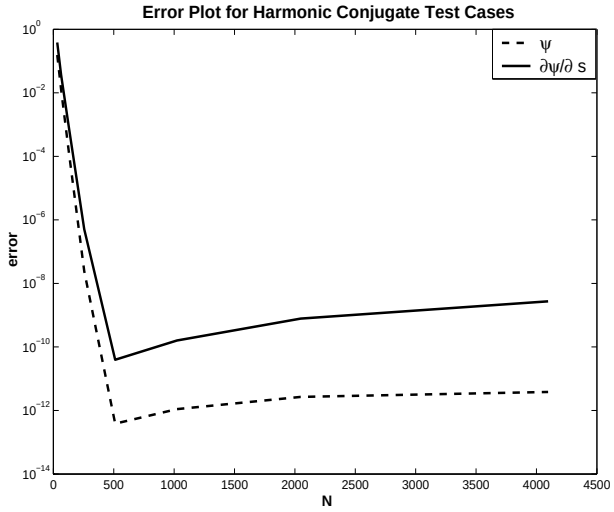

Figure 5.5: Errors for Harmonic Conjugate Test Cases, $a = 3, b = 1$

N	32	64	128	256	512	1024	2048	4096
$L_\infty \psi$	1.55e-1	1.28e-2	1.40e-4	2.44e-8	3.84e-13	1.10e-12	2.68e-12	3.84e-12
Ratio ψ	-	12.13	91.62	5,727	63,538	0.35	0.41	0.70
$L_\infty \frac{\partial \psi}{\partial s}$	3.83e-1	3.69e-2	8.41e-4	5.10e-7	3.96e-11	1.60e-10	7.78e-10	2.72e-9
Ratio $\frac{\partial \psi}{\partial s}$	-	10.36	43.90	1,650	12,869	0.25	0.21	0.29

Table 5.3: Error ratios for Harmonic Conjugate Test Cases, $a = 3, b = 1$

As seen from Figure 5.5 and Table 5.3, the results appear to converge super-algebraically to the exact solution as the mesh is refined. In general, the harmonic conjugate has a smaller error than the differentiated conjugate. This expected since Fourier differentiation results in a loss of accuracy of $\mathcal{O}(N)$, where N is the number of points used. In this case, this means a loss of accuracy $10^2 - 10^3$ when compared to the harmonic conjugate itself. This is exactly the behavior present in Figure 5.5 and Table 5.3.

These tests confirm the correct implementation of the Laplace solver into the existing Stokes solver. The program is now used to deal with the fully coupled fluid-electrostatic problem.

Chapter 6

Electrohydrodynamic Bubble Problem

The numerical solver is now applied to the electrohydrodynamic problem described in Chapter 2; namely, a conducting bubble within an unbounded viscous fluid subjected to a uniform electric field. This problem is the topic of examination of several recent papers. Crowdy [8] examines the two-dimensional problem discussed within the current study, motivated by an analogous three-dimensional problem examined in Dubash & Mestel [10]. While Dubash & Mestel perform a numerical investigation using boundary integral methods, Crowdy uses an analytical approach based on conformal mapping techniques coupled with a numerical method based on Laurent series expansions. The behavior of a variety of problems is investigated, including both compressible and incompressible bubbles in a very viscous flow, subject to both external electric fields and straining flows.

As discussed in [8], there appear to be no other papers investigating bubble problems where electrostatic effects are coupled to two-dimensional Stokes flow. Therefore, the current work aims to introduce a fast numerical method for solving Stokes flow problems coupled with Laplacian boundary value problems, in addition to verifying the validity of results presented by Crowdy.

6.1 Analytical Solution Method

The problem in [8] that relates to the current work is the behavior of an incompressible conducting bubble of fluid in an external unbounded viscous fluid, subject to a uniform electric field. This problem is described in the current study by (2.21)-(2.30). The approach taken by Crowdy is to proceed analytically as far as possible using conformal mappings and Laurent series expansions. A numerical method is resorted to only after all analytical means have been exhausted. Full details are found in [8], but the approach is briefly outlined here.

Note, as discussed in Crowdy, there is no possibility of the "Stokes Paradox" in this two-dimensional problem (where the solution of a three-dimensional Stokes flow problem has no corresponding solution in two-dimensions). Crowdy arrives at this conclusion from the simple fact that solutions to the two-dimensional problem are obtained numerically, implying well-posed solutions to the electrohydrodynamic problem actually exist.

6.1.1 Complex Variable Reformulation

The dimensionless governing equations and boundary conditions for the fluid dynamics, (2.21)-(2.30), are recast into a complex variable formulation. However, Crowdy's choices in this reformulation differ from those presented in Chapter 3. First of all, the roles of the vorticity and pressure are reversed in the definition of the Goursat function f, as compared to (3.2)

$$p - i\omega = 4f'(z).$$

The streamfunction is taken as the *imaginary* part of the function defined in (3.4)

$$\Psi(z) = \mathrm{Im}(\bar{z}f(z) + g(z)),$$

which leads to the following definitions, analogous to (3.5) and (3.10)

$$\begin{aligned} u + iv &= -f(z) + z\overline{f'(z)} + \overline{g'(z)}, \\ \tau_{11} + i\tau_{12} &= z\overline{f''(z)} + \overline{g''(z)}. \end{aligned}$$

As discussed in [22], there is some degree of arbitrariness in the selections made, but any choices result in an equivalent mathematical description of the problem. For example, the choices used in [8] are identical to those in [33], whereas the definitions used in Chapter 3 are identical to those presented in [20, 22]. In [20], several results from [33] are reproduced, showing an equivalence of the different choices.

Finally, the surface tension along the interface is assumed spatially constant in [8]. However, the approach used in Chapter 3 to describe spatially varying surface tension, (3.15), is still valid, with minor modification. As discussed in [14], the complex variable form of the spatially varying surface tension contribution to the dynamic boundary condition is unchanged from the form of the spatially constant version, save for a factor of σ. Since the surface tension σ is used for non-dimensionalizing the problem, the dimensionless forms are identical. Hence, no change is required in (3.15).

The resulting form of the dynamic boundary condition using Crowdy's notation is

$$f(z) + z\overline{f'(z)} + \overline{g'(z)} = -\frac{i\sigma}{2}\frac{\partial z}{\partial s} + \frac{\beta}{4}\int \left(\frac{\partial \phi}{\partial n}\right)^2 \frac{\partial z}{\partial s} ds. \tag{6.1}$$

6.1.2 Conformal Mapping

The mathematical treatment of the free boundary in [8] is significantly different than in the current study. A conformal mapping is introduced to rewrite both the electrostatic boundary value problem and the fluid problem into a form more amenable for analytic study. The interior of the unit circle in the complex ζ-plane, $|\zeta| = 1$, is mapped to the unbounded domain Ω exterior to the bubble interface $\partial\Omega$ in the complex z-plane. The mapping has the form

$$z(\zeta, t) = \frac{a(t)}{\zeta} + h(\zeta, t). \tag{6.2}$$

Here, the unknown function $a(t)$ is real-valued and $h(\zeta, t)$ is a complex-valued function that is analytic in the unit circle $|\zeta| = 1$. Therefore, it possesses a Taylor series representation of the form

$$h(\zeta, t) = \sum_{n=0}^{\infty} a_n(t)\zeta^n, \quad \text{for } |\zeta| = 1. \tag{6.3}$$

As the precise mathematical form of the boundary $\partial\Omega$ is unknown, the functions $a(t)$ and $h(\zeta, t)$ are unknown as well. The coefficients in the mapping, $a(t), a_n(t)$ are determined as part of the solution to the problem and are used to reconstruct the interface via (6.2).

The electrostatic boundary value problem is solved in the ζ-plane by writing the boundary value problem (2.24) in terms of ζ. Letting $\phi = \mathrm{Re}(\Phi)$, the solution within the unit disk $\zeta \leq 1$ is given in terms of the complex potential Φ

$$\Phi(\zeta, t) = a(t)\left(\frac{1}{\zeta} - \zeta\right). \tag{6.4}$$

With the introduction of the conformal mapping (6.2), the electrostatic problem is solved in the ζ-plane. Committing to this approach, the fluid problem is also reformulated in the ζ-plane. The details of the fluid mapping are discussed in several sources [8, 14, 31, 33] and only briefly summarized here.

The solution (6.4) is used in the dynamic boundary condition (6.1). Note that since $\mathbf{E} = -\nabla\phi$ in general, and on the bubble interface $\mathbf{E} = (\mathbf{E}\cdot\mathbf{n})\mathbf{n} \implies |\mathbf{E}|^2 = (\mathbf{E}\cdot\mathbf{n})^2$, the electric stress term along the interface is rewritten as

$$\begin{aligned}\frac{\beta}{2}\left(\frac{\partial\phi}{\partial n}\right)^2\mathbf{n} &= \frac{\beta}{2}\left(\nabla\phi\cdot\mathbf{n}\right)^2\mathbf{n}\\ &= \frac{\beta}{2}\left(\mathbf{E}\cdot\mathbf{n}\right)^2\mathbf{n}\\ &= \frac{\beta}{2}|\mathbf{E}|^2\mathbf{n}.\end{aligned}$$

Since $\phi = \mathrm{Re}(\Phi)$, use of $\mathbf{E} = -\nabla\phi$ and some algebraic manipulations leads to

$$\frac{\beta}{2}|\mathbf{E}|^2\mathbf{n} = \frac{\beta}{2}\left|\frac{d\Phi}{dz}\right|^2\mathbf{n}. \tag{6.5}$$

Upon substitution of (6.5) in (6.1), the dynamic boundary condition, evaluated along $|\zeta| = 1$, becomes

$$\begin{aligned}f(z) + z\overline{f'(z)} + \overline{g'(z)} &= -\frac{i\sigma}{2}\frac{\partial z}{\partial s} + \frac{\beta}{4}\int^s\left|\frac{d\Phi}{dz}\right|^2\frac{\partial z}{\partial s}ds\\ &= -\frac{i\sigma}{2}\frac{\partial z}{\partial s} + \frac{\beta}{4}\int^\zeta\frac{|d\Phi/d\zeta|^2}{\overline{\partial z/\partial\zeta}}d\zeta\\ &= -\frac{i\sigma}{2}\frac{\partial z}{\partial s} + \frac{\beta a^2(t)}{4}\int^\zeta\frac{(1+\zeta^2)^2}{\zeta^2(\overline{\partial z/\partial\zeta})}d\zeta.\end{aligned} \tag{6.6}$$

The remaining terms in (6.6) are rewritten as functions of ζ using the definitions $F(\zeta) = f(z(\zeta,t),t)$, $G(\zeta) = g'(z(\zeta,t),t)$ and the identity

$$\frac{\partial z}{\partial s} = \frac{i\zeta\partial z/\partial\zeta}{|\partial z/\partial\zeta|}$$

which is valid on $|\zeta| = 1$. Following the approach found in [8, 33], (6.6) becomes

$$2G(\zeta)\frac{\partial z}{\partial\zeta} = -2\overline{F(\zeta)}\frac{\partial z}{\partial\zeta} - \overline{z}\frac{\partial F}{\partial\zeta} + \frac{|\partial z/\partial\zeta|}{\zeta} + \frac{\beta a^2(t)}{2}\frac{\partial z}{\partial\zeta}\overline{\int^\zeta\frac{(1+\zeta^2)^2}{\zeta^2\overline{\partial z/\partial\zeta}}d\zeta}. \tag{6.7}$$

The kinematic boundary condition, (2.28), is also reformulated in terms of ζ

$$\frac{dz}{dt} + 2F(\zeta) = \zeta\frac{\partial z}{\partial\zeta}I(\zeta), \tag{6.8}$$

where

$$I(\zeta) = \frac{1}{2\pi i} \oint_{|\zeta'|=1} \frac{d\zeta'}{\zeta'} \left(\frac{\zeta' + \zeta}{\zeta' - \zeta} \right) \left[\frac{1}{2|\partial z/\partial \zeta|} + \mathrm{Re} \left[\frac{r(\zeta')}{\zeta' \partial z/\partial \zeta} \right] \right]. \tag{6.9}$$

Here $r(\zeta)$ is given by the integral term in (6.6).

The main equations governing the flow are the modified dynamic boundary condition (6.7) and the kinematic boundary condition (6.8). The equations are too complicated to admit an analytical solution, so a numerical approach is used instead. The functions F, G are given series representations within $|\zeta| \leq 1$. Arguments defining each choice are found in [14, 33]. The representations are

$$\begin{aligned} F(\zeta) &= \frac{F_{-1}}{\zeta} + \sum_{n=0}^{\infty} F_n \zeta^n, \\ G(\zeta) &= \sum_{n=0}^{\infty} G_n \zeta^n. \end{aligned} \tag{6.10}$$

In each case the coefficients in (6.10) are unknown. These representations are substituted into (6.7). As described in [8], the series are then truncated to 64 terms each, leading to a finite system of equations for the unknown coefficients. The process used to solve for these coefficients is complicated and not repeated here, but full details are found in [3, 32]. Once the coefficients are determined, they are used in (6.8) to obtain differential equations for the evolution of the coefficients of the conformal mapping, $a(t), a_n(t)$. These coefficients are evolved forward in time to obtain the location of the interface, thereby solving the free-boundary value problem.

6.2 Crowdy's Results

Using the numerical method described above, Crowdy reports the following findings on the bubble dynamics. Noting that in Crowdy's notation $E^2 = \beta$ from (2.27), the bubble has two states, characterized by the dimensionless parameter $E = \sqrt{\beta}$, and a critical value, E_{crit}.

6.2.1 Sub-Critical Case

For $E < E_{crit}$, after an initial transient period, the bubble evolves to reach an essentially elliptical fixed equilibrium profile. Physically, the externally applied electric field is not strong enough to overcome the surface tension forces present along the bubble interface. The dynamics are dominated by surface tension effects and the bubble attains a fixed profile.

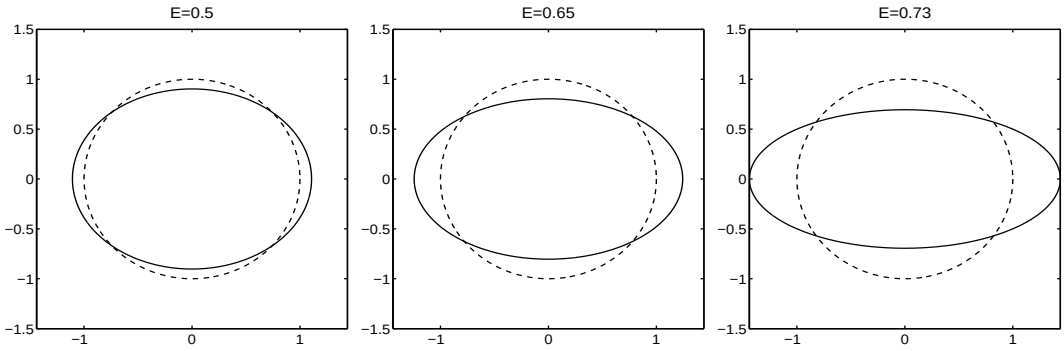

Figure 6.1: Equilibrium bubble profiles evolving from an initially circular profile, showing $E = \sqrt{\beta} = 0.5, 0.65, 0.73$.

Through numerical experimentation, Crowdy calculates the aspect ratio of the maximum steady-state elliptical bubble to be $e = 0.455$, where e is the ratio of the semi-major axis to the semi-minor axis. This occurs at a critical parameter value of approximately $E_{crit} = 0.745$.

Based on the results of this equilibrium case, a simplified evolution model for the bubble profile is derived. According to simulations, the bubble profiles are very nearly elliptical. Crowdy modifies the conformal mapping, (6.2), to map from the interior of the unit circle to the exterior of an ellipse

$$z(\zeta, t) = \frac{a(t)}{\zeta} + b(t)\zeta. \tag{6.11}$$

This mapping allows the exact evaluation of the integral contribution in the dynamic boundary condition, (6.6), and results in a set of evolution equations for the unknown coefficients a and b in (6.11). Defining $e = b/a$, or $a = 1/\sqrt{1-e^2}$, $b = e/\sqrt{1-e^2}$, a single non-linear ordinary differential equation is obtained for the time evolution of e

$$\frac{de}{dt} = \left(\frac{1-e^2}{1+e^2}\right)\left(\frac{\beta}{6}(2-2e-e^2) - 2e\hat{I}_0\right), \tag{6.12}$$

where $\hat{I}_0 = I_0 + \beta I_1$ is given by the following integrals

$$\begin{aligned} I_0 &= \frac{1}{4\pi i}\oint_{|\zeta|=1} \frac{d\zeta}{\zeta}\frac{1}{|\partial z/\partial\zeta|}, \\ I_1 &= \frac{1}{2\pi i}\oint_{|\zeta|=1} \frac{d\zeta}{\zeta}\mathrm{Re}\left(\frac{\tilde{r}(\zeta)}{\zeta(\partial z/\partial\zeta)}\right). \end{aligned}$$

Using a parametric form on $|\zeta| = 1$ given by $\zeta = e^{i\nu}$ with $\nu \in [0, 2\pi]$, the integral I_0 is

rewritten as an elliptic integral of the first kind [2], denoted by the function K

$$\begin{aligned} I_0 &= \frac{1}{4\pi i}\oint_{|\zeta|=1}\frac{d\zeta}{\zeta}\frac{1}{|\partial z/\partial\zeta|} \\ &= \frac{1}{\pi}\sqrt{\frac{1-e}{1+e}}K\left(\frac{4e}{(1+e)^2}\right). \end{aligned} \tag{6.13}$$

This result is valid for $0 \leq e \leq 1$, which is the case for an initially circular bubble being stretched horizontally by an externally applied electric field.

In I_1, the function $\tilde{r}(\zeta)$ is defined in terms of the integral

$$\begin{aligned} \tilde{r}(\zeta) &= \frac{\beta a^2(t)}{4}\int_1^{\zeta}\frac{(1+\zeta^2)^2}{\zeta^2(b-a\zeta^2)}d\zeta \\ &= -\frac{a}{4}\left(\zeta+\frac{a}{b\zeta}+\sqrt{\frac{a}{b}}\frac{(a+b)^2}{2ab}\log\left(\frac{1-\sqrt{b/a}\zeta^{-1}}{1+\sqrt{b/a}\zeta^{-1}}\right)\right)+C \\ &= -\frac{1}{4\sqrt{1-e^2}}\left(\zeta+\frac{1}{e\zeta}+\frac{(1+e)^2}{2e^{3/2}}\log\left(\frac{1-\sqrt{e}\zeta^{-1}}{1+\sqrt{e}\zeta^{-1}}\right)\right) \\ &+ \frac{1}{4\sqrt{1-e^2}}\left(1+\frac{1}{e}+\frac{(1+e)^2}{2e^{3/2}}\log\left(\frac{1-\sqrt{e}}{1+\sqrt{e}}\right)\right) \end{aligned}$$

This model is used to evaluate the shape of the bubble for sub-critical β values. Crowdy reports no significant difference between the full numerical method and this evolution model for the sub-critical case. Therefore, it provides a simple way for obtaining solutions in the sub-critical case.

The evolution model is used to predict the critical E value below which the sub-critical case exists. By taking the evolution equation (6.12) and solving for the equilibrium solution, $\dot{e} = 0$, the remaining terms are reorganized to give the field strength in terms of the parameter e

$$E^2 = \frac{12eI_0}{(2-2e-e^2)-12eI_1}. \tag{6.14}$$

This relationship produces the plot in Figure 6.2, which is in turn used to determine the critical field strength predicted by the evolution model.

As indicated in Figure 6.2, the critical field strength is given by $E_{crit} = 0.7372$. This differs from the prediction of $E_{crit} = 0.745$ in Crowdy's full numerical model by $\mathcal{O}(10^{-2})$. As discussed in [8], this is consistent with the error involved in assuming the conformal mapping between the exterior of the bubble and the interior of the region in the ζ-plane is exactly elliptical.

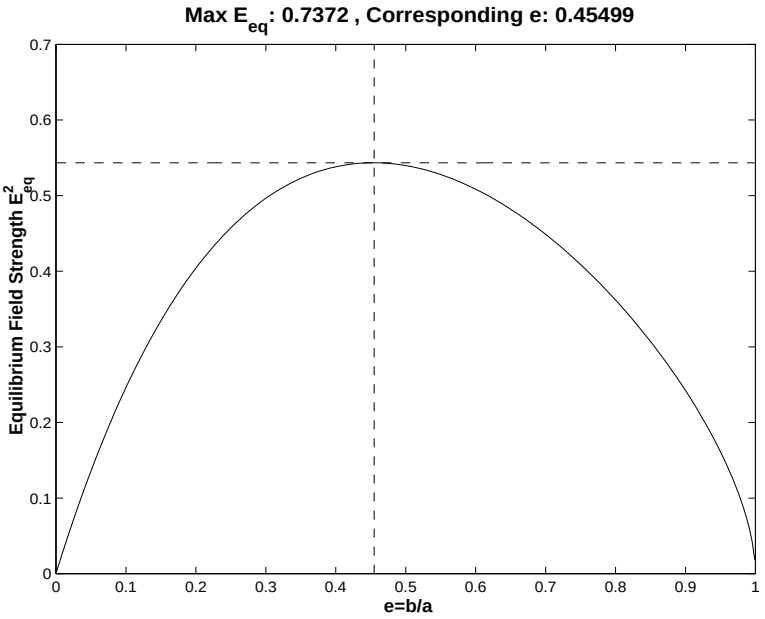

Figure 6.2: Graph of E^2 vs. e showing critical equilibrium value of $E = \sqrt{\beta}$=0.7372.

6.2.2 Super-Critical Case

For $E > E_{crit}$, there is no reported equilibrium profile. The applied electric field is strong enough to overcome the restorative surface tension forces along the bubble interface. The electric field acts to continually stretch the bubble until "pinch-off" occurs in the center of the bubble, effectively splitting it into two segments. The evolution equation (6.12) does not apply to the super-critical case, as the bubble is no longer elliptical and the conformal mapping, (6.11), is not valid. In addition, the mathematical model used fails to apply after pinch-off, as its topology changes to that of a multiply connected region.

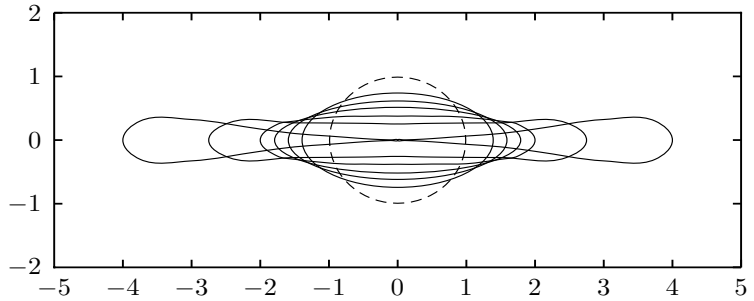

Figure 6.3: Non-equilibrium bubble profile for super-critical case.

6.3 Numerical Test Cases and Comparison

The numerical solver is used to investigate both the sub-critical and super-critical cases reported by Crowdy. The results stated above are used as a reference for computed solutions obtained with the solver.

6.3.1 Sub-Critical Case

For the sub-critical case, the numerical solver is able to reproduce the results presented in [8] with some notable differences. Mainly, the β values for equilibrium solutions differ from those reported by Crowdy. As an example, the solver is used to recreate the first image in Figure 6.1 ($E = 0.5$) for comparison with the evolution model in (6.12). The result is illustrated in Figure 6.4.

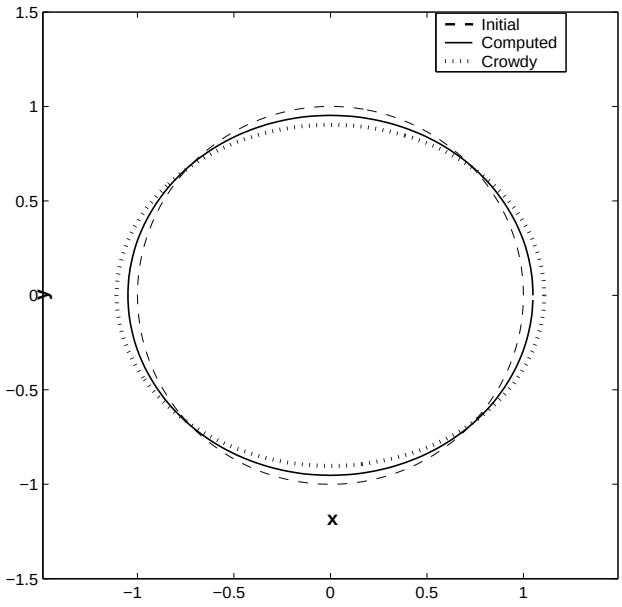

Figure 6.4: Comparison of computed profile vs. Crowdy model, $E = \sqrt{\beta} = 0.5$.

The computed profile disagrees with the evolution model. The solver underpredicts the horizontal deformation of the bubble, as seen in Figure 6.4. However, the numerical solver is able to reproduce the correct profile using a different β value, suggesting that there is a difference in scalings used for the non-dimensionalizations presented in this work and in [8].

Although defined identically, the values of β and E^2 are not equivalent for a given set of parameters. The difference is explained by noting that in [8], the area of the initial circular bubble is used in defining the length scale. The radius of the bubble, r, is used as the characteristic length R in (2.27), giving

$$E^2 = \frac{\varepsilon_0 E_0^2 r}{\sigma_0}.$$

However, as discussed in Chapter 2, the characteristic length scale associated with the numerical solver is based upon the diameter, $D = 2r$, of the initial circular bubble, giving

$$\begin{aligned} \beta &= \frac{\varepsilon_0 E_0^2 D}{\sigma_0} \\ &= \frac{\varepsilon_0 E_0^2 (2r)}{\sigma_0}. \end{aligned}$$

These scalings lead to a factor of two difference in the value of the parameters E^2 and β, implying that $\beta = 2E^2$, or $\sqrt{\beta} = \sqrt{2}E$. To verify this, numerical experimentation is used to compute several pairs of β and E values corresponding to the same bubble profile. These values are plotted in Figure 6.5.

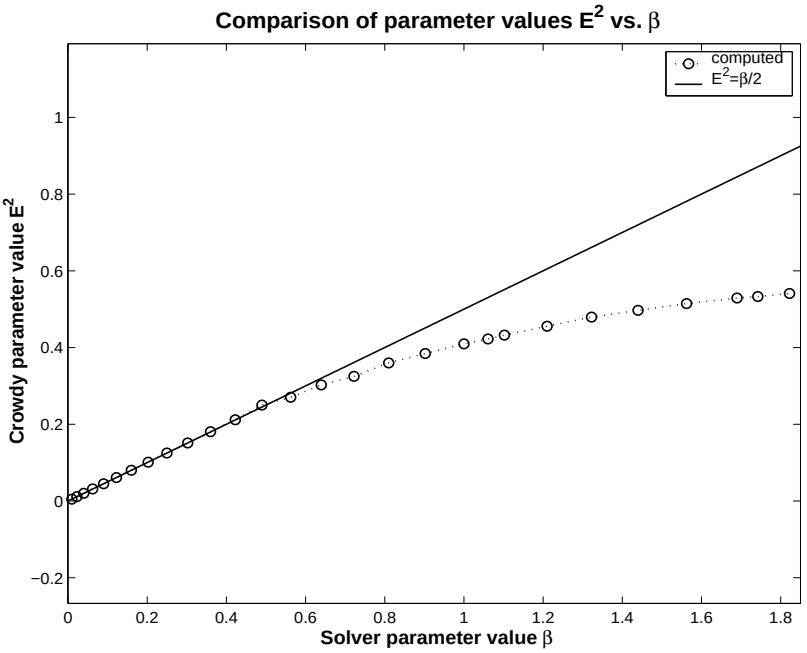

Figure 6.5: Scaling relationship between solver and evolution model.

As seen in Figure 6.5, for $\beta < 0.60$ there is excellent agreement between β and E values and the function $E^2 = \frac{1}{2}\beta$. This suggests that the length scale argument correctly accounts for the difference in the parameter values and bubble profiles for relatively low values of β. The parameter value used in the numerical solver is modified according to the above discussion in order to reproduce bubble profiles from the evolution model. This is illustrated in Figures 6.6, 6.7, and 6.8.

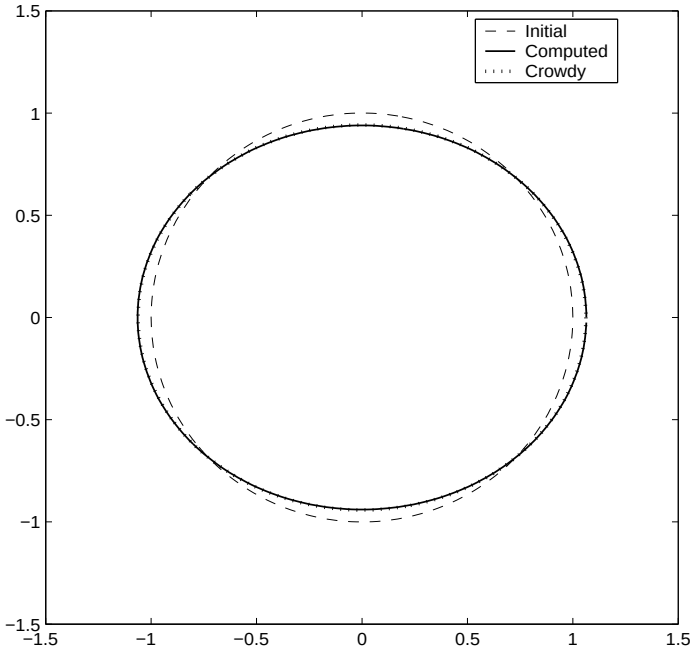

Figure 6.6: Comparison of Crowdy model, $E = 0.40$ vs. computed profile, $\sqrt{\beta} = 0.566$.

There is very good agreement between the results of the numerical solver and the evolution model. The profiles in Figures 6.6 and 6.7 are nearly indistinguishable, verifying that the scaling argument discussed above is correct. The profiles deviate slightly in Figure 6.8, but this is expected as $\sqrt{\beta} = 0.849$, or $\beta = 0.72$, falls in the non-linear region of Figure 6.5. The deviation is more pronounced the larger the parameter becomes and the closer E is to E_{crit}. This is illustrated in Figure 6.9. The reason for this deviation and the non-linear behavior in Figure 6.5 is unknown. The numerical solver is able to match profiles produced by the evolution model in this parameter range, but it is unclear as to why the constant scaling factor is no longer valid. However, based on these results, the numerical solver is able to accurately reproduce the results of the sub-critical evolution model presented in [8].

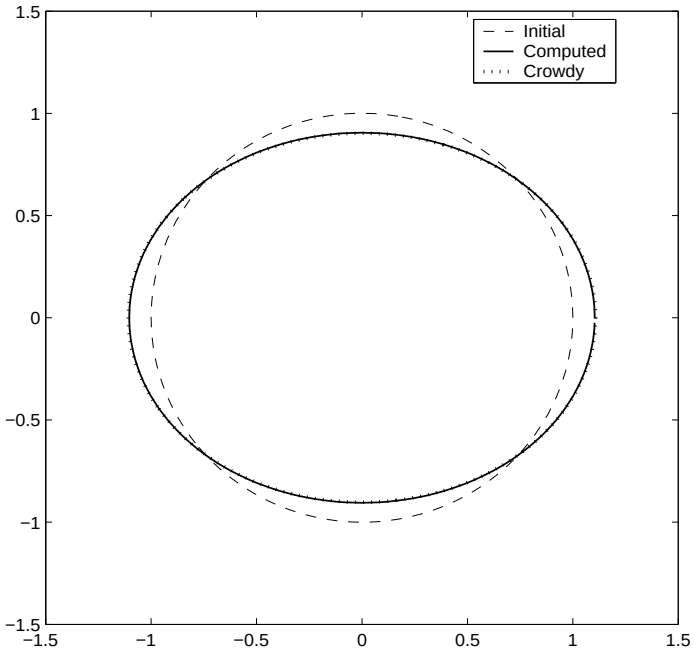

Figure 6.7: Comparison of Crowdy model, $E = 0.50$ vs. computed profile, $\sqrt{\beta} = 0.707$.

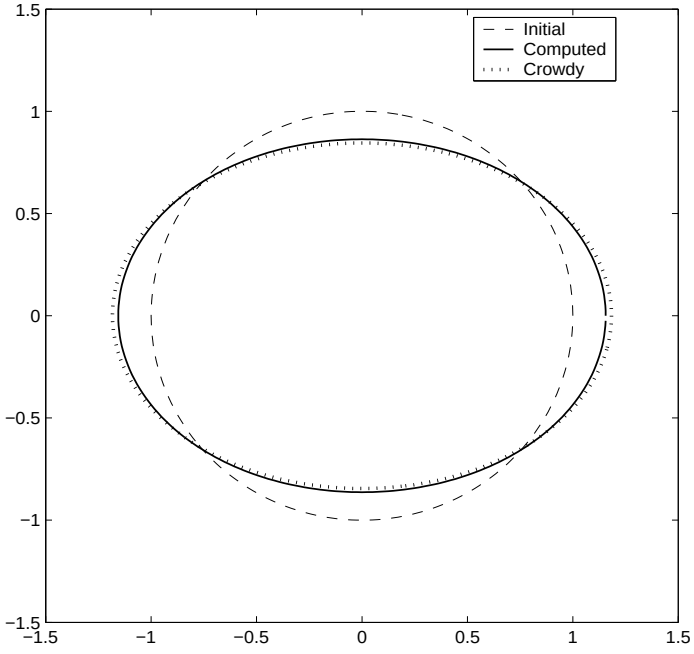

Figure 6.8: Comparison of Crowdy model, $E = 0.60$ vs. computed profile, $\sqrt{\beta} = 0.849$.

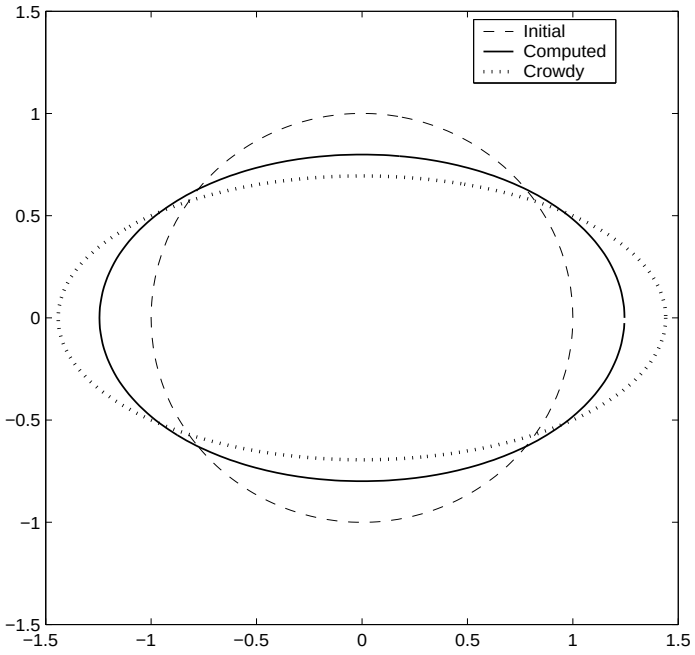

Figure 6.9: Comparison of Crowdy model, $E = 0.73$ vs. computed profile, $\sqrt{\beta} = 1.032$.

For reference, CPU times for the computation of one time step in the sub-critical case are listed in Table 6.1. In this table, the time step is $\Delta t = 0.001$ seconds, and an initial elliptical profile corresponding to $E = 0.73$ or $\sqrt{\beta} = 1.32$ is used. This corresponds to an ellipse with $a = 1.44$ and $b = 0.6942$, parameterized as in Chapter 5.3.1.

N	32	64	128	256	512	1024	2048	4096
CPU time (s)	4.063e-1	5.156e-1	7.188e-1	1.250	2.172	3.969	8.250	18.250

Table 6.1: CPU times for elliptical bubble profile, $a = 1.44$, $b = 0.6942$, $\Delta t = 0.001$.

Another difference between the solver and the evolution model lies in the ellipticity assumption made in [8]. Specifically, the validity of the elliptic conformal mapping, (6.11), is in question. As the value of β increases, the equilibrium profiles begin to deviate from elliptical. This behavior is evident when comparing the computed results to purely elliptical profiles. For small β values, there is negligible deviation between the two, as seen in Figures 6.6 and 6.7. However, the profiles deviate further as β increases, and the result is more pronounced the larger β is increased. This behavior is illustrated by the equilibrium solution for $\beta = 9.0$ in Figure 6.10.

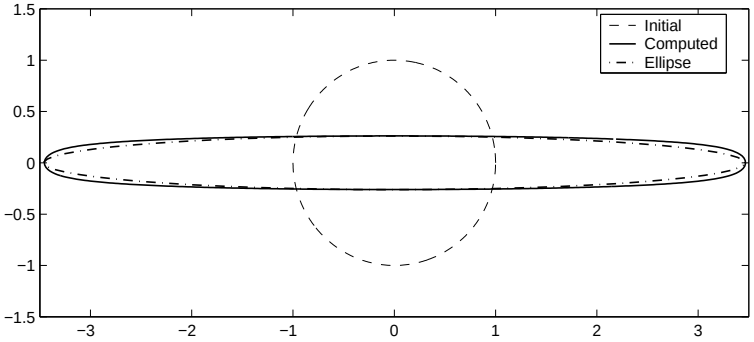

Figure 6.10: Comparison of computed profile for $\beta = 9.0$ and an ellipse.

At higher parameter values there is significant deviation between the computed result and the elliptic profile. This suggests that the assumption of an elliptical bubble profile is not valid for equilibrium solutions at higher β values and implies there may be other profile shapes in the equilibrium regime. This needs to be investigated further.

As a final difference between the current work and the results reported in [8], numerical experimentation with the solver shows that equilibrium solutions are achieved for parameter values up to $\beta \approx 15$. In this case, the maximum aspect ratio is $e \approx 0.03$, which is well below the maximum ratio of 0.455 reported by Crowdy. This aspect ratio produces an equilibrium profile which is far more deformed than the profile corresponding to the maximum aspect ratio obtained by Crowdy, as illustrated in Figure 6.11.

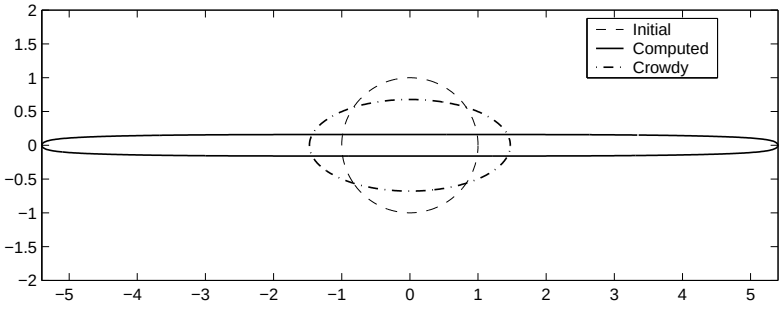

Figure 6.11: Comparison of maximum equilibrium profiles. Computed, $\beta = 15.0$ vs. Crowdy, $E = 0.7372$.

6.3.2 Super-Critical Case

As discussed in [8], above a given β, the bubble does not achieve an equilibrium profile. The applied electric field causes the bubble to continually deform until the profile pinches-off. Crowdy reports that this occurs for $E = \sqrt{\beta} > E_{crit} \approx 0.745$. As discussed above, the results of the numerical solver disagree with this value. The bubble profiles exhibit non-equilibrium behavior for $\beta > 15$. The computed profiles are non-elliptical and pinch-off at the center, as seen in Figure 6.12. This pinch-off occurs for all β values above critical.

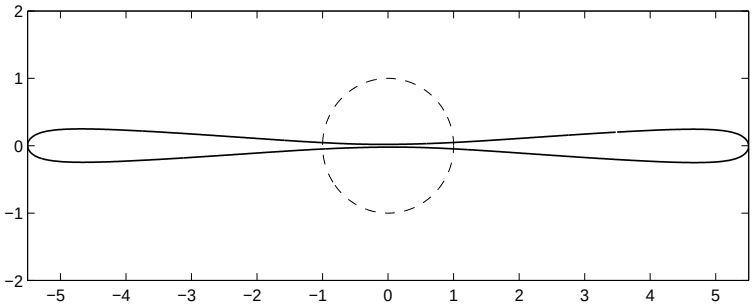

Figure 6.12: Computed profiles showing bubble pinch-off, $\beta = 50$, $N = 1024$.

The result computed in [8] corresponding to Figure 6.3 is for $E = 0.80$. However, there is no way of determining the corresponding β value for the numerical solver, so at best there is only qualitative agreement between the computed solution and the result in [8].

It is worth noting that all computed solutions with $\beta > 15$ lead to the same spatial profile, namely Figure 6.12. This behavior cannot be compared with any results in [8] as there is no further mention of the bubble dynamics in the super-critical case. For instance, does the result in [8] corresponding to Figure 6.3 apply for all $E > E_{crit}$, or does the spatial profile of the bubble change with E? If Crowdy's model has the same spatial profile for all $E > E_{crit}$, then there is a quantitative difference in the computed profile in Figure 6.12 and the result corresponding to Figure 6.3. Comparing the profiles, the maximum spatial extent of the computed bubble profile is $x \approx \pm 5.5$, while in Crowdy's result, the extent is $x \approx \pm 4$. This difference may be due to the scaling issue discussed earlier. However, further investigation is necessary.

These results suggest a successful implementation of the numerical solver. Based on comparisons to previously reported results, the solver is able to compute full solutions to the electrohydrodynamic bubble problem.

Chapter 7

Conclusion and Future Work

7.1 Conclusion

This thesis develops a fast and efficient numerical method for solving electrohydrodynamic free boundary problems. Specifically, the method calculates the interfacial profile of a single two-dimensional electrically conducting bubble within an infinite expanse of viscous fluid. The bubble and fluid are subjected to an externally applied uniform electric field. The motion of the bubble is in the creeping flow regime. The governing fluid equations are the linear Stokes equations, which are amenable to mathematical analysis. The electrostatic potential of the system is governed by Laplace's equation. The governing equations in the fluid domain and the appropriate boundary conditions are initially stated in a primitive variable formulation, then rewritten in terms of complex potential functions. These equations, in turn, are recast as integral equations along the bubble interface. This approach converts the solution of the primitive variable equations in an infinite domain into the solution of integral equations along the bubble boundary.

The integral equations are discretized using a spectrally accurate method and solved with an iterative solver accelerated by the fast-multipole method. This computes the solution of the discrete electrohydrodynamic problem in $\mathcal{O}(N)$ floating-point operations, where N is the number of points used to the discretize the interface. The numerical solver is validated against several analytic results. This method provides a fast and efficient means of computing free boundary electrohydrodynamic problems.

The solver is used to track the interface of a conducting bubble in a viscous fluid subject to an electric field. Existing analytic results show that the dynamics of the bubble are

controlled by a single dimensionless parameter, representing the ratio of electric stresses to surface tension stresses along the bubble interface. In particular, the bubble either reaches an equilibrium profile for sufficiently small parameter values, or deforms in a non-steady fashion until a "pinch-off" in the profile occurs for the case of larger parameter values.

The numerical solver reproduces these results; namely a steady-state quasi-elliptic profile, and a transient profile that evolves until "pinch-off". The computed steady-state profiles are compared to a simplified analytic evolution model. The computed solutions reproduce the analytic results, but at different parameter values than those predicted by the analytic model. The results differ by a scaling factor, due to a difference in the non-dimensionalizations used in the analytic result and the current study. The non-equilibrium profiles agree qualitatively with previously reported results, showing the "pinch-off" behavior. Based on these results, the numerical method succeeds in providing a fast and efficient method for computing free-boundary electrohydrodynamic problems.

7.2 Future Work

In the context of the electrostatic boundary value problem, this study deals only with the solution of Laplace's equation subject to Dirichlet boundary conditions. An obvious generalization of the method is to consider either Neumann boundary conditions or mixed boundary conditions. This is easily accommodated within the integral equation framework presented here. However, the integral representations for these cases involve *single-layer potentials*. As with the double-layer potential, the kernel of the single-layer potential is singular along a boundary. Unfortunately, for a single-layer potential, in the limit as the singular point is approached there is no convenient representation in terms of a continuous function, as was the case with the double-layer potential and the interface curvature. Further research is required into how to represent and discretize this case.

Once these alternate boundary conditions are implemented, the numerical solver can be applied to other problems involving coupled physical processes. For example, a problem of interest is the motion of a surfactant-laden bubble in a straining Stokes flow with diffusion of surfactant off of the bubble interface. The diffusion is governed by Laplace's equation and a mixed boundary condition is used to couple the surfactant concentration to the fluid problem at any given time.

The method presented here is applicable to single bubbles only. However, it can be

modified to deal with multiple bubbles. This modification would require additional terms in both the fluid and electrostatic models to deal with the multiple interfaces. Regardless of the number of bubbles, the discrete model would still lead to the solution of a system of equations and can be dealt with using the existing approach. The new system would simply be augmented by additional equations. This approach is discussed in [21] for Stokes flow problems, and [16] for Laplacian boundary value problems.

Bibliography

[1] M.J. Ablowitz and A.S. Fokas. *Complex Variables, Introduction and Applications*. Cambridge Texts in Applied Mathematics. Cambridge University Press, 2003.

[2] M. Abramowitz and I.A. Stegun. *Handbook of Mathematical Functions with Formulas, Graphs, and Mathematical Tables*. Dover Publications, ninth edition, 1970.

[3] L.K. Antanovskii. Quasi-steady deformation of a two-dimensional bubble placed within a potential viscous flow. *Meccanica*, 29:27–42, 1994.

[4] K. Atkinson and Y. Jeon. Algorithm 788: Automatic boundary integral equation programs for the planar laplace equation. *ACM Transactions on Mathematical Software*, 24:395–417, 1998.

[5] G.F. Carrier, M. Krook, and C.E. Pearson. *Functions of a Complex Variable, Theory and Technique*. Classics in Applied Mathematics. SIAM, 2005.

[6] J. Carrier, L. Greengard, and V. Rokhlin. A fast adaptive multipole algorithm for particle simulations. *SIAM J. Sci. Statist. Comput.*, 9, 1988.

[7] D.K. Cheng. *Field and Wave Electromagnetics*. Addison-Wesley: Reading, Massachusetts, second edition, 1992.

[8] D. Crowdy. Conducting drops subject to electric fields in 2d stokes flows. *IMA Journal of Applied Mathematics*, 73:740–758, 2008.

[9] N. Dubash and A.J. Mestel. Behavior near critical for a conducting drop in an electric field. *Physics of Fluids*, 19:073104, 2007.

[10] N. Dubash and A.J. Mestel. Behavior of a conducting drop in a highly viscous fluid subject to an electric field. *J. Fluid Mech.*, 581:469–493, 2007.

[11] N. Dubash and A.J. Mestel. Breakup behavior of a conducting drop suspended in a viscous fluid subject to an electric field. *Physics of Fluids*, 19:072101, 2007.

[12] L.C. Evans. *Partial Differential Equations*, volume 19 of *Graduate Studies in Mathematics*. American Mathematical Society, 1998.

[13] G.B. Folland. *Introduction to Partial Differential Equations.* Princeton University Press, 1998.

[14] J.R.P Gilmore. The calculation of interface motion of a surfactant-laden bubble in stokes flow. Master's thesis, Simon Fraser University, 2003.

[15] G. Goranovic. *Electrohydrodynamic aspects of two-fluid microfuidic systems: theory and simulation.* PhD thesis, Mikroelektronik Centret (MIC) Technical University of Denmark, 2003.

[16] A. Greenbaum, L. Greengard, and G.B. McFadden. Laplace's equations and the dirichlet-neumann map in multiply connected domains. *J. Comp. Phys.*, 105:627–278, 1993.

[17] T.Y. Hou, J.S. Lowengrub, and M.J. Shelley. Removing the stiffness from interfacial flows with surface tension. *J. Comp. Phys.*, 114:312–338, 1994.

[18] O.D. Kellogg. *Foundations of Potential Theory.* Dover Publications, 1953.

[19] M.C.A. Kropinski. Integral equation methods for particle simulations in creeping flows. *Computers and Mathematics with Applications*, 38:67–87, 1999.

[20] M.C.A. Kropinski. An efficient numerical method for studying interfacial motion in two-dimensional creeping flows. *Journal of Computational Physics*, 171:479–508, 2001.

[21] M.C.A. Kropinski. Numerical methods for multiple inviscid interfaces in creeping flows. *Journal of Computational Physics*, 180:1–24, 2002.

[22] W.E. Langlois. *Slow Viscous Flow.* Macmillan, 1964.

[23] J. Levandosky. Stanford math 220b lecture notes. Summer 2003.

[24] E. Lushi. A fast numerical method for the interfacial motion of a surfactant-laden bubble in creeping flow. Master's thesis, Simon Fraser University, 2006.

[25] G.B. McFadden, P.W. Voorhees, R.F. Boisvert, and D.I. Meiron. A boundary integral method for the simulation of two-dimensional particle coarsening. *Journal of Scientific Computing*, 1(2), 1986.

[26] S.G. Mikhlin. *Integral Equations.* International Series of Monographs in Pure and Applied Mathematics. Pergamon Press, 1957.

[27] N.I. Muskhelishvili. *Singular Integral Equations.* Noordhoff Press, 1958.

[28] C. Pozrikidis. *Boundary Integral and Singularity Methods for Linearized Viscous Flow.* Cambridge Texts in Applied Mathematics. Cambridge University Press, 1992.

[29] C. Pozrikidis. *Introduction to Theoretical and Computational Fluid Dynamics.* Oxford University Press: New York, Oxford, 1997.

[30] J.D. Sherwood. The deformation of a fluid drop in a electric field: a slender-body analysis. *J. Phys. A: Math. Gen.*, 24:4047–4053, 1991.

[31] M. Siegel. Influence of surfactant on rounded and pointed bubbles in two-dimensional stokes flow. *SIAM J. Appl. Math.*, 59:1998–2007, 1999.

[32] M. Siegel. Cusp formation for time-evolving bubbles in two-dimensional stokes flow. *J. Fluid Mech.*, 412:227–257, 2000.

[33] S. Tanveer and G.L. Vasconcelos. Time-evolving bubbles in two-dimensional stokes flow. *J. Fluid Mech.*, 301:325–344, 1995.

[34] L.N. Trefethen. *Spectral Methods in MATLAB*. SIAM, 2000.

[35] L.N. Trefethen and D. Bau. *Numerical Linear Algebra*. SIAM, 1997.

[36] F.G. Tricomi. *Integral Equations*. Dover Publications, 1985.

[37] C. T. R. Wilson and G. I. Taylor. The bursting of soap bubbles in a uniform electric field. *Proc. Camb. Phil. Soc.*, 22:728–730, 1925.